Decriem, J., Árnadóttir, T., Hooper, A., Geirsson, H., Sigmundsson, F., Keiding, M., Ófeigsson, B. G., Hreinsdóttir, S., Einarsson, P., LaFemina, P., Bennett, R. A. (2010): The 2008 May 29 earthquake doublet in SW Iceland. - Geophysical Journal International, 181, 2, 1128-1146

DOI: 10.1111/j.1365-246X.2010.04565.x

Geophysical Journal International

Geophys. J. Int. (2010) **181**, 1128-1146 doi: 10.1111/j.1365-246X.2010.04565.x

The 2008 May 29 earthquake doublet in SW Iceland

J. Decriem,[1] T. Árnadóttir,[1] A. Hooper,[2] H. Geirsson,[3] F. Sigmundsson,[1] M. Keiding,[1] B. G. Ófeigsson,[1] S. Hreinsdóttir,[4] P. Einarsson,[1] P. LaFemina[5] and R. A. Bennett[4]

[1] *Nordic Volcanological Center, Institute of Earth Sciences, University of Iceland, IS-101 Reykjavík, Iceland. E-mail: judicael@hi.is*
[2] *Delft Institute of Earth Observation and Space Systems (DEOS), Delft University of Technology, Delft, Netherlands*
[3] *Physics Department, Icelandic Meteorological Office, Reykjavík, Iceland*
[4] *Department of Geosciences, University of Arizona, Tucson, AZ, USA*
[5] *Department of Geosciences, Pennsylvania State University, University Park, PA, USA*

Accepted 2010 February 13. Received 2010 February 11; in original form 2009 November 17

SUMMARY

On 2008 May 29 an earthquake doublet shook the southwestern part of Iceland. The first main shock originated beneath Mt Ingólfsfjall, located near the western margin of the South Iceland Seismic Zone (SISZ) approximately 40 km east of the capital Reykjavík. Immediate aftershock activity was recorded by the SIL seismic network, operated by the Icelandic Meteorological Office (IMO), with both N-S and E-W structures illuminated over a broad area. A continuous GPS (CGPS) network, also operated by the IMO, recorded coseismic offsets with up to 200 mm of horizontal motion at the closest stations. We estimate the coseismic surface deformation observed by campaign and continuous GPS and satellite radar data (InSAR). We invert the geodetic data to find the optimal geometry, location and slip on the main faults, accounting for variation in the elastic parameters of the crust with depth. Our models indicate that most of the slip occurred on two N-S structures spaced ~5 km apart. From a joint inversion of GPS and InSAR data for variable slip models we find that most of the slip for the first (Ingólfsfjall) event was concentrated at 2-4 km depth with a maximum of 1.9 m, whereas the slip on the second (Kross) fault was located deeper, at 3-6 km depth with up to 1.4 m of motion. The models give similar geodetic moments for the two main events, equivalent to a moment magnitude of M_w5.8 and M_w5.9 for the first and second event, respectively. Our estimated composite moment therefore equals a M_w6.1 for the doublet, smaller than the M_w6.3 estimated from teleseismic data (e.g. NEIC and Harvard).

The geodetic data support rupture on two main faults and analysis of high-rate (1 Hz) CGPS data suggests that slip on the second fault initiated within 3 s of the first main shock. Static Coulomb failure stress calculations indicate that the first event caused a stress increase in the area of the main asperity (i.e. at the location of the largest slip patch) on the second fault. However, we cannot rule out dynamic stress triggering due to the short time between the two main events. The 2008 May 29 earthquake doublet appears to be a continuation of the earthquake sequence that started in 2000 June, when two M_w6.5 events struck the eastern and central part of the South Iceland Seismic Zone, in the span of 81 hr. The 2000 June-2008 May sequence has released about half of the moment accumulated by plate motion since the previous earthquake sequence in 1896-1912. Therefore, continued earthquake activity with moderate size events rupturing N-S faults in the SISZ in the coming decades is likely.

Key words: Satellite geodesy; Space geodetic surveys; Earthquake source observations; Seismicity and tectonics.

1. INTRODUCTION

Iceland is the largest subaerial part of the Mid-Atlantic Ridge, the boundary between the North American and Eurasian plates. The rate of plate divergence across Iceland is ~19 mm yr^{-1} causing major seismic and volcanic activity in the island. The Reykjanes Peninsula is the onshore extension of the Reykjanes Ridge in southwest Iceland, characterized by oblique spreading as the direction of relative plate motion deviates by ~30° from the trend of the plate boundary axis. The Hengill triple junction marks the intersection of the Reykjanes Peninsula (RP), the Western Volcanic Zone (WVZ) extending to the north, and the South Iceland Seismic Zone (SISZ) (Fig. 1). The SISZ is an approximately 80-km-long E-W transform zone accommodating left-lateral shear, due to the plate spreading in South Iceland. The eastern end of the SISZ joins the Eastern Volcanic Zone (EVZ), where

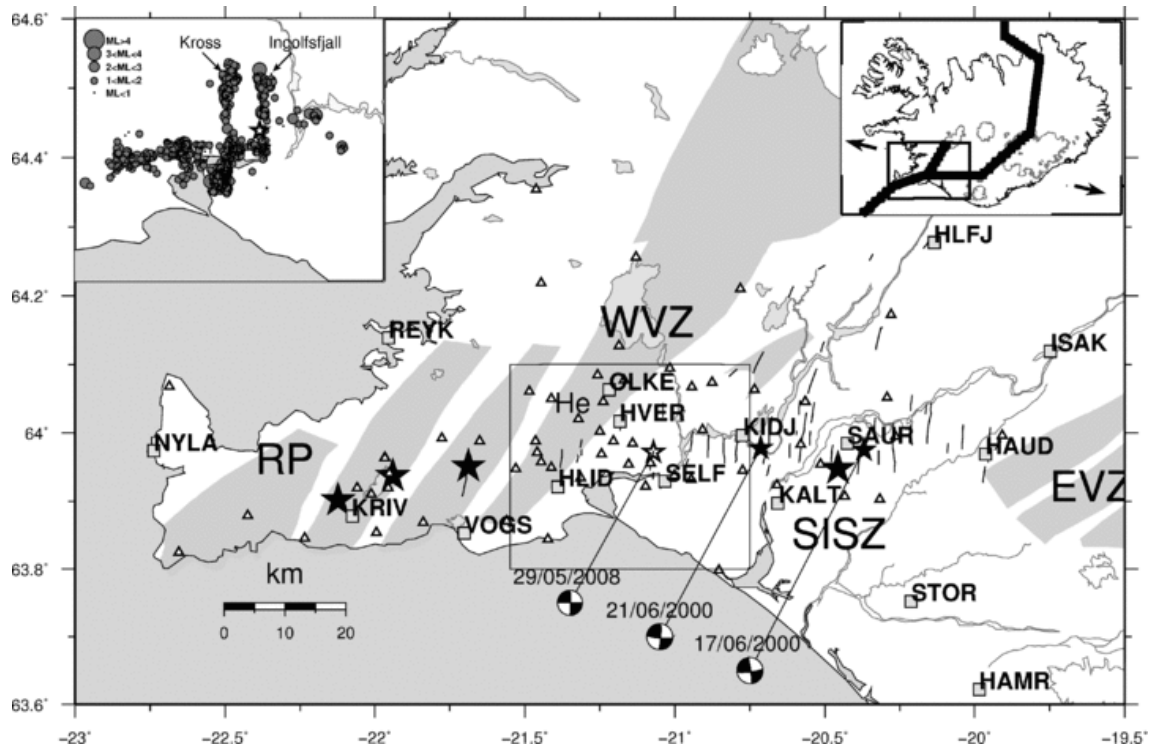

Figure 1. The main tectonic features in the study area: the Reykjanes Peninsula (RP), the Hengill triple junction (He), the Western and Eastern Volcanic Zones (WVZ and EVZ, respectively) and the South Iceland Seismic Zone (SISZ). Individual fissure swarm are shown in light grey. The stars indicate the epicentres of M_w > 5 events in 2000 June (black) and the initial 2008 May 29 main shock (white). The focal mechanisms are from the USGS. The white triangles denote GPS campaign sites and grey squares the continuous GPS stations. The right-hand inset shows the plate boundary across Iceland and the location of the study area is indicated with a rectangle. The black arrows show the plate spreading according to the NUVEL-1A plate motion model (*DeMets et al.* 1994). The inset to the left-hand side shows the epicentre of 2008 May 29 main shock (white star) and aftershocks (grey circles) recorded by the SIL seismic network from 2008 June 2 to 2008 July 10. The circles are scaled to represent the local magnitude (M_L).

most of the extension across south Iceland is currently taking place.

The SISZ is characterized by arrays of N-S right lateral strike-slip faults, spaced 2-5 km apart (*Einarsson* 1991; *Clifton & Einarsson* 2005). Each of the N-S faults is composed of an array of left stepping en echelon surface fractures, separated by push-up structures (e.g. *Bjarnason et al.* 1993b; *Clifton & Einarsson* 2005). Earthquake activity in south Iceland has been recorded by the SIL seismic network (*Stefánsson et al.* 1993) operated by the IMO, since 1989. Micro-earthquakes (down to magnitude less than zero) have been used to map active fault surfaces at depth (*Hjaltadóttir* 2009). Studies following the 2000 June earthquake sequence indicate that the larger faults are nearly vertical, planar features extending to approximately 10 km depth, although complicated fracture patterns have in some cases been mapped at the surface (e.g. *Clifton & Einarsson* 2005; *Hjaltadóttir* 2009).

Global Positioning System (GPS) observations have been used to document crustal deformation in Iceland since 1986 (*Foulger et al.* 1987). A network of continuous GPS (CGPS) stations, operated by the Icelandic Meteorological Office (IMO), has been expanding since 1999 (*Geirsson et al.* 2006). Many previous geodetic studies in SW Iceland address plate spreading (e.g. *Hreinsdóttir et al.* 2001; *LaFemina et al.* 2005; *Árnadóttir et al.* 2006; *Keiding et al.* 2008), while others focus on earthquake deformation (e.g. *Árnadóttir et al.* 2001; *Pedersen et al.* 2001, 2003; *Jónsson et al.* 2003; *Pagli et al.* 2003; *Árnadóttir et al.* 2004; *Jónsson* 2008; *Sudhaus & Jónsson* 2008). *LaFemina et al.* (2005) used GPS campaign measurements between 1992 and 2003 to infer latitudinal variation in the spreading rates across the WVZ and the EVZ, the two main axes of spreading in south Iceland. From 2-D modelling of these GPS measurements *LaFemina et al.* (2005) suggested a rate decrease along the WVZ, from 7.0 mm yrr^{-1} in the south to 2.6 mm yrr^{-1} in the northern part of the zone, and an increase in rates along the EVZ from 11 mm yrr^{-1} in the south to 19 mm yrr^{-1} in the north. *LaFemina et al.* (2005) also concluded that the sum of the extension rates across the WVZ and the EVZ is 18-20 mm yr^{-1}, in the direction of plate motion (N102°E), which is consistent with plate motion model predictions (*Sella et al.* 2002). The crustal deformation due to relative plate motion in southwest Iceland has been estimated from GPS measurements between 1992 and 2004 by *Árnadóttir et al.* (2006). In this study, the 2000 pre-June GPS station velocities in SW Iceland were modelled assuming that the plate boundary can be approximated with several vertical dislocations. The study estimated a locking depth of ~15 km and a deep slip rate of around 19 mm yrr^{-1} for the SISZ.

The accommodation of E-W shear at depth in the SISZ by motion on a series of parallel N-S faults, causing counter-clockwise rotation of blocks, has been termed 'bookshelf faulting' (*Einarsson et al.* 1981; *Sigmundsson et al.* 1995). Sequences of earthquakes in the SISZ have been documented in historical records, for example in 1732-1734, 1784 and 1896 (*Einarsson et al.* 1981; *Stefánsson & Halldórsson* 1988). During the 1896 sequence at least five events larger than magnitude 6 were reported

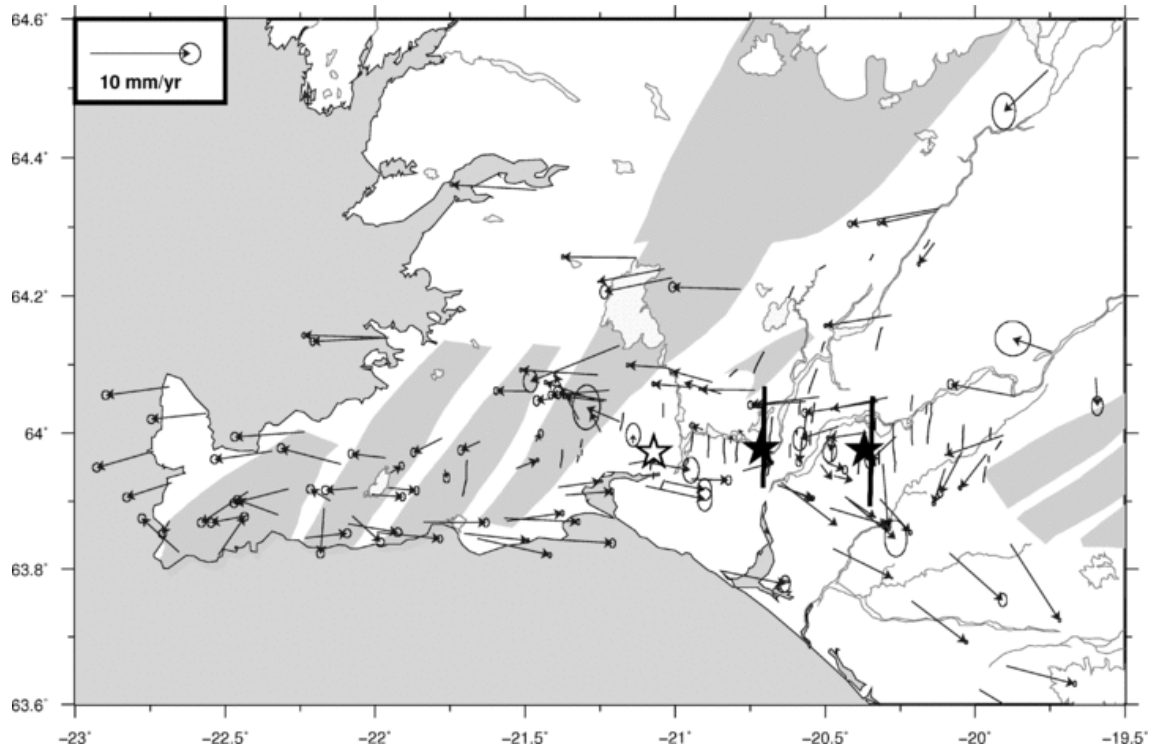

Figure 2. GPS station velocities (with 95 per cent confidence ellipses) in the SISZ and Reykjanes Peninsula calculated from campaign and continuous observations form 2001 January 1 to 2008 May 28. The velocities are the average between the solutions for stable North America and stable Eurasia, to depict motion relative to the plate boundary. The stars show the 2000 June main shocks (black) and the initial 2008 May 29 main shock (white). The black bold lines are the surface projections of the variable slip models for the 2000 June events (*Pedersen et al.* 2003).

over a distance of 50 km within two weeks. The largest instrumentally recorded earthquake was a $M_S = 7.0$ event which struck the eastern part of the SISZ in 1912 (*Bjarnason et al.* 1993a; *Bellou et al.* 2005). A new earthquake sequence in the SISZ was initiated on 2000 June 17 with a main shock of magnitude $M_w = 6.5$ in the east-central part, followed 81 hr later by another $M_w = 6.5$ event, located 17 km west of the June 17 main shock. The surface deformation caused by the June 17 and 21 main shocks was measured using both GPS and Interferometric Synthetic Aperture Radar (InSAR). Modelling of the geodetic data suggests up to 2.5 m of slip on two parallel 10 km long N-S faults (*Árnadóttir et al.* 2001; *Pedersen et al.* 2001, 2003). Three $M_w > 5$ events were triggered along the plate boundary on the Reykjanes Peninsula, up to 80 km from the June 17 main shock (*Pagli et al.* 2003; *Vogfjörd* 2003). One of these events caused a water level drop of several metres of Lake Kleifarvatn (*Clifton et al.* 2003). Triggering of the secondary events has been studied using the slip models derived from geodetic data to estimate the dynamic and static coseismic Coulomb stress changes (*Árnadóttir et al.* 2003, 2004; *Antonioli et al.* 2006). Observations of rapid postseismic deformation have been explained by models of poro-elastic rebound (*Jónsson et al.* 2003). Although the static stress changes following the June 17 main shock promote failure on the June 21 fault these models do not explain the 81 hr delay between the two main events. Stress changes due to fluid flow following the first main shock may explain the time delay (*Lindman* 2009).

Here we study the surface deformation caused by the May 29 earthquake doublet. We consider these events a continuation of the sequence that started in the SISZ in 2000 June. The 2008 May 29 sequence initiated with a main shock beneath the Ingólfsfjall mountain (63.972°N, 21.072°W and ~5 km depth) at 15:45:58.9 UTC according to the SIL seismic catalogue (IMO). Almost immediately, aftershock activity started on a second fault (the Kross fault), located approximately 5 km west of the initial main shock. Increased earthquake activity was also observed along an E-W zone, with several M_L3 events (Fig. 1). The teleseismic centroid-moment-tensor solutions indicate rupture on a near vertical fault, with right lateral motion on a N-S striking fault or left-lateral motion on an E-W oriented structure, with a seismic moment of $M_w6.3$ (NEIC). Coseismic offsets were observed by the CGPS network in the area (*Hreinsdóttir et al.* 2009), and campaign style GPS measurements were started a few hours after the initial main shock (*Decriem et al.* 2008). The earthquake sequence was also observed by the ICEARRAY strong motion network (*Halldórsson & Sigbjörnsson* 2009).

Independent estimates of the coseismic offsets causing the 2008 May 29 earthquakes at CGPS stations in SW Iceland have been used to model the fault geometry and slip by *Hreinsdóttir et al.* (2009). Here we extend the work by *Hreinsdóttir et al.* (2009) by analysing campaign and continuous GPS data as well as radar interferograms (InSAR). The dense spatial sampling of InSAR data combined with the 3-D GPS displacements improve the constraints on the model parameters from the previous study. We invert the geodetic data to estimate dislocation source geometries and locations, and distribution of slip on the rupture surfaces using a layered half-space rheology to account for heterogeneities of the elastic parameters in the

Icelandic crust. From our extensive geodetic data set we are able to resolve variations in the slip models on a 500 m gridded plane. The variation of the elastic parameters with depth does not greatly affect the fault geometry, but is important when estimating coseismic stress changes. Our Coulomb failure stress calculations indicate an agreement between areas of stress increase and locations of aftershocks.

2. DATA

2.1 GPS data and analysis

Annual campaign style GPS measurements have been conducted in the SISZ and on the Reykjanes Peninsula since 2000 June (*Árnadóttir et al.* 2006; *Keiding et al.* 2008). During the campaign measurements each site is normally occupied for at least one 24 hr session. We resurveyed 52 benchmarks in a GPS campaign between 2008 April 29 and May 19. Following the May 29 earthquakes, all benchmarks within a radius of ~100 km that we had previously occupied with GPS, were remeasured (Fig. 1). In addition, we deployed a semi-continuous GPS network where 21 benchmarks were occupied almost continuously until July 21 and 12 stations until mid-August.

In order to estimate the inter and coseismic deformation in SW Iceland we include in our analysis all available campaign and continuous GPS data from 2001 to 2008.

The GPS data analysis is performed in two steps. First, we calculate daily solutions using the Bernese v5.0 software (*Dach et al.* 2007) with orbit information and Earth rotation parameters from the International GPS Service (IGS) in the International Terrestrial Reference Frame (ITRF) 2005. For each 24 hr session we include the GPS campaign data, CGPS data from stations in Iceland, and data from nine long-running CGPS stations outside of Iceland (ALBH, ALGO, ALRT, BRUS, CAGL, DREJ, MADR, ONSA and WES2). The processing includes (1) cycle slip correction from phase single difference, (2) double-difference phase residuals screening and outlier rejection, (3) coordinates and troposphere estimates using the Quasi Ionosphere Free (QIF) strategy and (4) final coordinate estimation, zenith path delays and horizontal tropospheric gradient based on the L3 linear combination. In this last procedure the coordinates of the nine fiducial sites outside of Iceland are tightly constrained by means of a three parameter Helmert transformation (the three translation components should be zero and the residuals below 1 cm).

In the second step, we import SINEX files containing the Bernese daily solutions into the GLOBK software (*Herring et al.* 2006) to generate a solution using a regional stabilization approach (*McClusky et al.* 2000). We first combine our solutions with three IGS global network solutions (IGS1, IGS3, and EURA) using the global stations in the origin definition. We then identify the most stable fiducial sites as ALBH, ALGO, ALRT, MADR, ONSA, BRUS, CAGL and DREJ (misfit less than 1.23 mm in position and less than 0.5 mm yrr^{-1} in velocity) and realize a reference frame approximately aligned with the ITRF2005. Finally, we estimate annual positions and velocities with respect to the reference frame (Fig. 2).

We calculate the coseismic station displacements in east, north, and vertical by combining the time-series from 2001 January 1 to 2008 May 28 with the solution from 2008 May 30 to June 10. Fig. 3 shows the time-series from CGPS stations in the epicentral area. The benchmarks HV08, VG13, VG15, VG20, VG22 and VG24 had only been measured once with GPS, in 2007 November by the Iceland GeoSurvey (ISOR). In order to calculate the coseismic displacements at these sites, we need to estimate the interseismic velocities in order to correct for the 6 months of plate motion between 2007

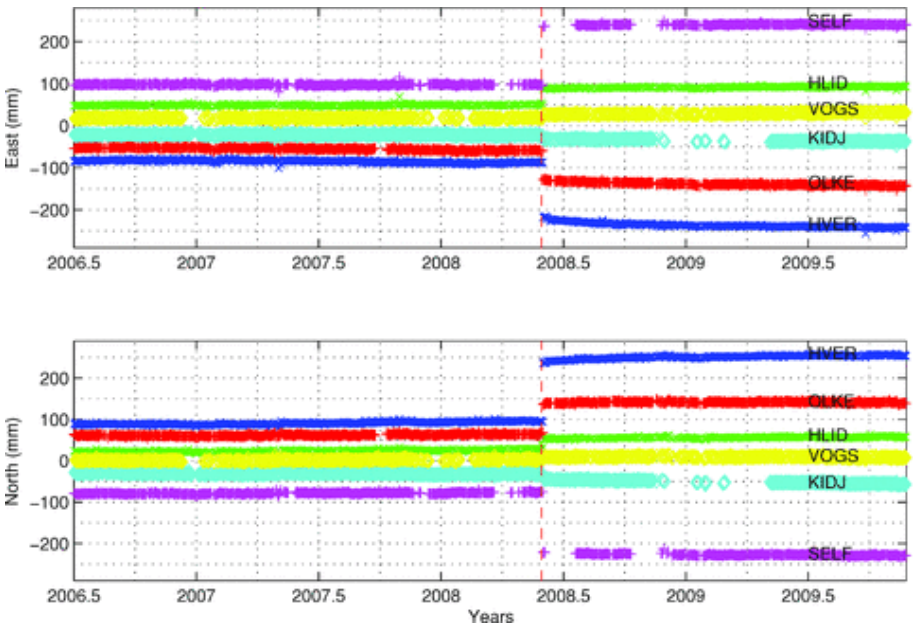

Figure 3. Continuous GPS time-series at the closest stations to the Ingólfsfjall area corrected for plate motion and seasonal effects. The coseismic displacements are seen as offsets on the time-series on 2008 May 29 (indicated with a vertical dashed line).

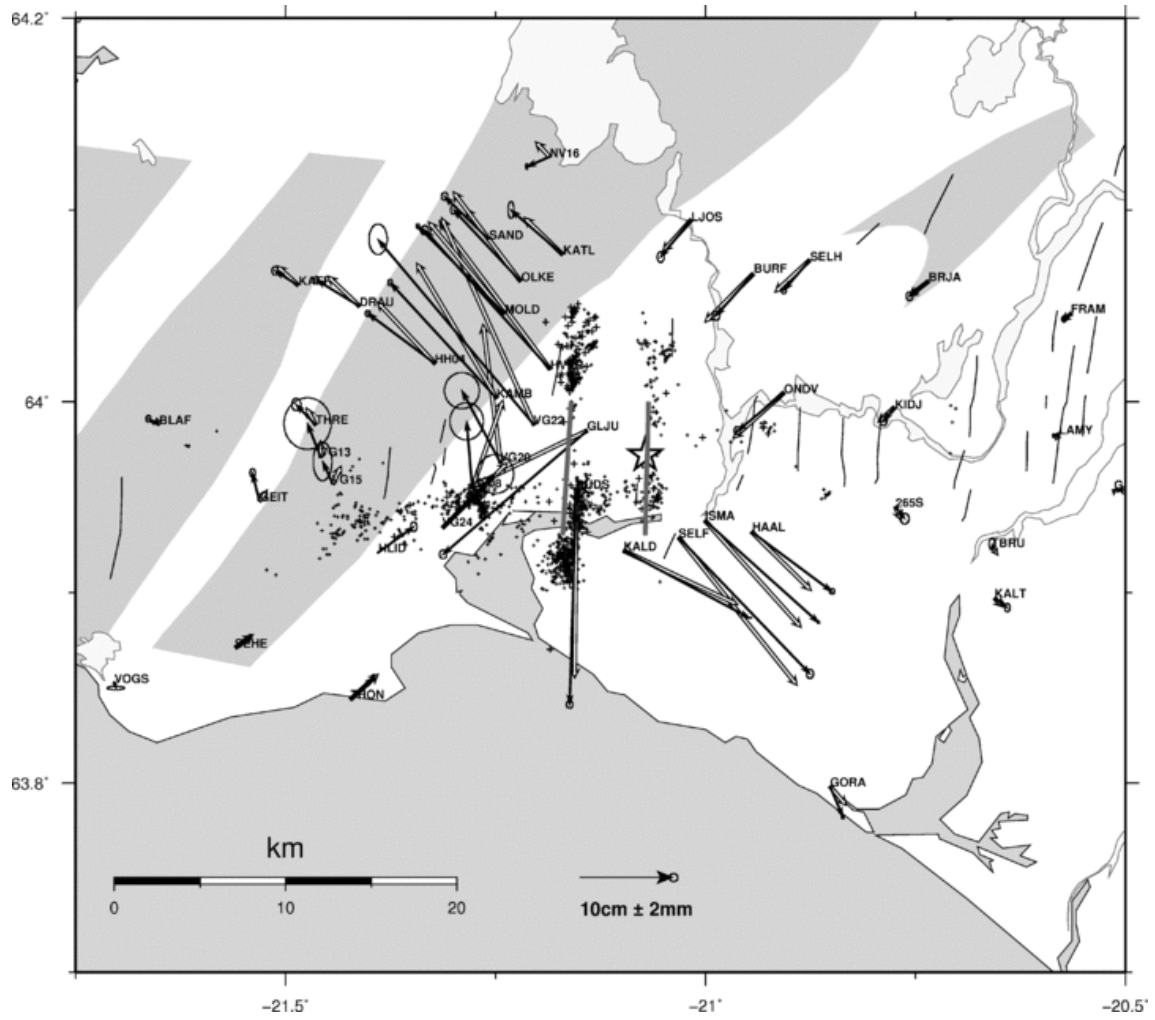

Figure 4. Coseismic deformation in the Ölfus area following the 2008 May 29 earthquake sequence. The observed horizontal GPS displacements are shown with black arrows and 95 per cent confidence ellipses, whereas the white arrows are the predicted displacements for the preferred uniform slip model (thick grey lines). The white star indicates the epicentre of the first main shock and black crosses show locations of aftershocks recorded by the SIL seismic network from 2008 June 2 to July 10.

November and 2008 May. The interseismic deformation is evaluated by interpolating the velocities at the closest station (THRE, GEIT, HLID and HVER) using a Delaunay triangulation scheme. The coseismic deformation observed by GPS is shown in Fig. 4 and the numerical values are given in Table S1. The large uncertainties in the coseismic estimates for the ISOR stations are due to short observation sessions in 2007 (each station was only observed for 2-6 hr) and the uncertainties in estimating the interseismic deformation.

2.2 InSAR data analysis

Interferometric Synthetic Aperture Radar (InSAR) is a satellite based method that can be used to measure surface deformation. When two images have been acquired with approximately the same observation geometry, it is possible to get a measurement of the surface displacement by differencing the phases of two SAR images. The advantage of InSAR is the dense spatial coverage associated with remote sensing, but because of the observation geometry, the surface deformation is only sampled along one direction, that is, the line-of-sight (LOS) of the radar. Several radar images acquired by ENVISAT and ALOS satellites span the time of the 2008 May earthquakes both along ascending and descending tracks (Table S2). The ASAR instrument onboard the ENVISAT satellite operates in C-band with a wavelength of 56.2 mm, whereas the PALSAR instrument onboard the ALOS satellite operates in L-band with a wavelength of 236.0 mm.

We use the Stanford Method for Persistent Scatterer (StaMPS) (*Hooper et al.* 2007) to generate interferogram time-series from 2007 to 2008 for three ENVISAT tracks, two descending (T138, T367) and one ascending (T402) in addition to an ascending ALOS track (T20). The mean LOS unit vector, $\hat{\boldsymbol{n}}$ = [East, North, Up], for each interferogram is: $\hat{\boldsymbol{n}}_{\mathrm{ALOS}}$ = [-0.62 -0.12 0.77], $\hat{\boldsymbol{n}}_{\mathrm{T138}}$ = [0.33 -0.09 0.93], $\hat{\boldsymbol{n}}_{\mathrm{T367}}$ = [0.36 -0.11 0.92] and $\hat{\boldsymbol{n}}_{\mathrm{T402}}$ = [-0.35 -0.10 0.92]. We use the time-series analysis to isolate the best target pixels (those most coherent in time) as well as to estimate the spatially correlated look angle errors (i.e. not randomly distributed errors due to spatially correlated errors in the DEM) and master atmosphere/orbit errors. The unwrapped phase is calculated with a statistical cost flow algorithm as described in *Hooper* (2009). From this analy-

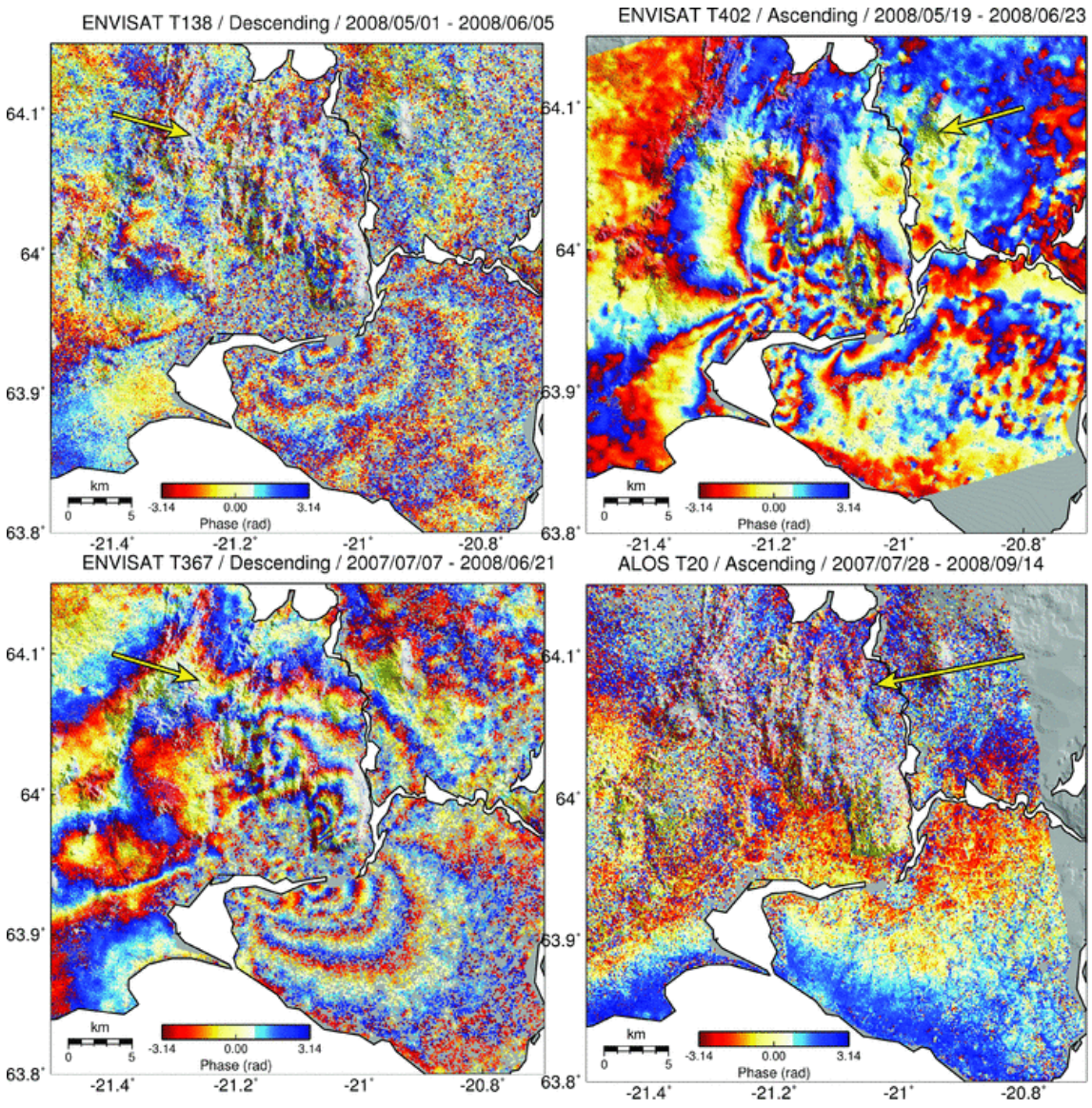

Figure 5. Wrapped phase interferograms spanning the 2008 May 29 earthquakes. Each colour cycle represents 28 mm of motion in the LOS between the ground and the ENVISAT satellite and 120 mm for the ALOS. The yellow arrows show the surface projection of the mean LOS unit vectors.

sis we select four interferograms with different sensors and observation geometries shown in Figs 5 and 6. The details of the available interfograms are given in Table S2.

2.2.1 *Error estimates for the InSAR data*

Several error sources affect the InSAR data, in the observation itself or due to the processing. The main sources of errors are electronic noise from the instrument, atmospheric disturbance along the radar wave paths, distribution of the scatterers for a given pixel, satellite orbit inaccuracies and digital elevation model (DEM) errors. The StaMPS method accounts for several error terms including uncorrelated noise, spatially correlated look angle errors (almost entirely due to DEM errors), and atmospheric and orbit errors due to the master image (*Hooper et al.* 2007). The remaining error terms in our data set mainly depend on the state of the atmosphere and ground surface conditions at acquisition time of the slave image. These errors are spatially correlated due to the smooth variation of the atmospheric signal delays and are specific for each interferogram. As the data interpretation and modelling depend on the quality of the measurements, we need to quantify the remaining error in the InSAR data. We do this by statistically estimating the empirical covariance function of each interferogram, following (*Sudhaus & Jónsson* 2008). We assume that the error statistics are the same across the whole image. Therefore, we can estimate the covariance function, cov(h), where h is the pixel separation distance in the nondeforming part of the interferogram and assume the same power and structure for the deforming part.

To estimate the covariance we first form a discrete semivariogram $\hat{\gamma}$ by sampling our data in the following manner:

$$\hat{\gamma}(h_c) = \frac{1}{2N}\sum_{i=1}^{N}[d(\boldsymbol{r}_i) - d(\boldsymbol{s}_i)]^2 \quad (1)$$

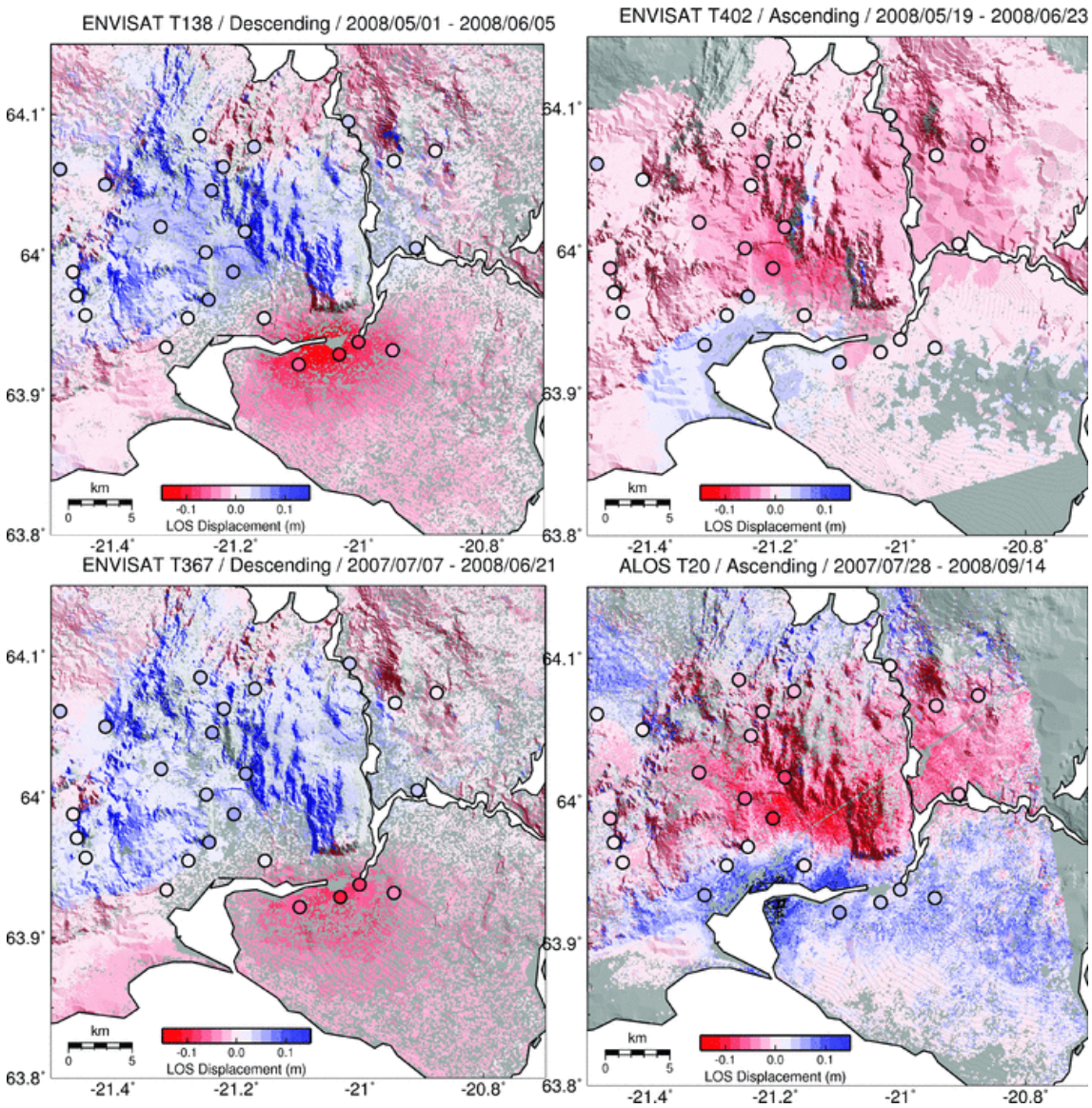

Figure 6. Unwrapped InSAR interferograms. The LOS displacements during the time interval given on each interferogram are shown by colour, where blue indicates an increase in the LOS (motion away from the satellite, primarily subsidence) and red represents a LOS decrease (motion towards the satellite). The coloured dots give the GPS station displacements projected onto the unit vector of the LOS for each interferogram.

where h_c is a bin of distances, $d(\boldsymbol{r}_i)$ and $d(\boldsymbol{s}_i)$ are the data values of the pixels located at r_i and s_i, and N is the number of pixels satistifying the distance $\|\boldsymbol{r}_i - \boldsymbol{s}_i\| \simeq h_c$. We use a bin width of h_c = 150 m ranging from 0 km to the half of the maximum separation possible and randomly sample 500 000 pixel pairs in the non-deforming part of our images to build $\hat{\gamma}(h_c)$. We then fit the semivariogram with an appropriate empirical function, $\gamma(h)$, given the shape of the variogram and the expected structure of the errors. Here, we assume that $\gamma(h)$ is an exponential decay function, $\gamma(h) = \sigma^2 \cdot \exp\left(\frac{-h}{a}\right)$, where a is the correlation length and σ^2 are the data variance.

Finally, we obtain the empirical covariance function from

$$\mathrm{cov}(h) = \mathrm{cov}(0) - \gamma(h), \qquad (2)$$

where $\mathrm{cov}(0)$ is the non-correlated error of each measurement, referred to as the semi-variogram zero crossing. Using eq. (2) we can calculate the full data covariance matrix for the interferograms given the separation distance between each pixel pair.

2.2.2 *Sub-sampling of the InSAR datasets*

Due to the extensive spatial coverage, the InSAR data sets consist of several hundred thousand points. We therefore need to resample our interferograms to a more manageable data set. We use an adaptive quadtree subsampling scheme similar to *Jónsson et al.* (2002) in order to reduce the number of data points without losing the benefits of the high spatial resolution of the radar images. The quadtree algorithm recursively divides the image into squares until the variance of the pixels contained in each square does not exceed a given threshold. Therefore, an area with a high variance will be subdivided whereas an area with a

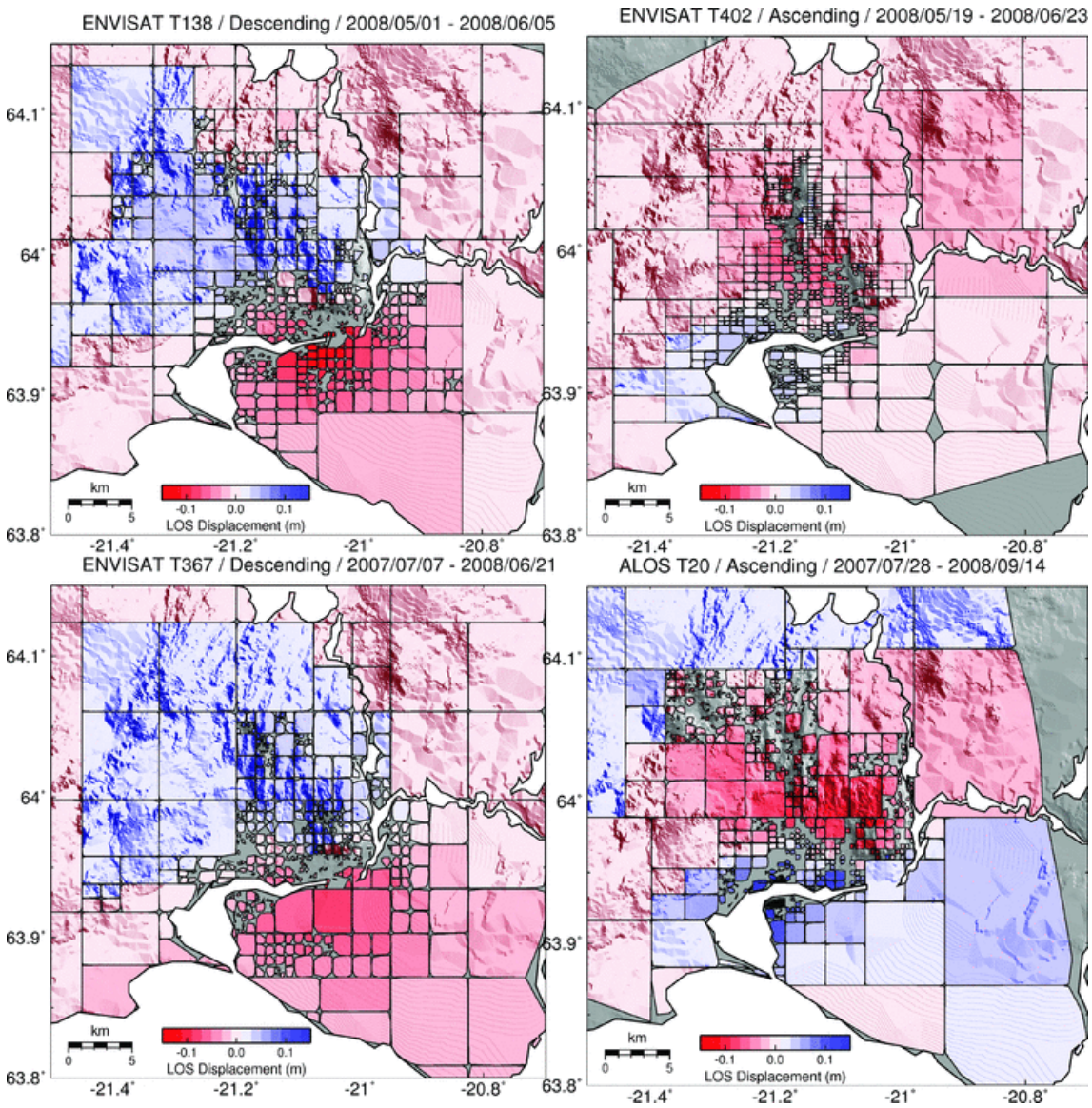

Figure 7. Quadtree subsampling of the LOS InSAR data.

low variance will be represented by larger squares. The quadtree algorithm adapts the subsampling to both the variance of the measurements and the spatial coverage in case of data gaps. Since StaMPS works with a list of persistent scatterer (PS) pixels rather than an array of pixels we apply the quadtree algorithm to the geographic coordinates (latitude and longitude) rather than the radar coordinates (range and azimuth). We define our 'squares' (or polygons in this case) as the spatial envelope around a group of PS pixels and the mean of all the geographic coordinates as the focal point. This strategy implies that our polygons can be irregularly aligned, depending on the density of points in a particular area. As a benefit, we note that using this approach reduces slightly the number of subdivisions caused by data gaps, especially along the edges of the image. We set the threshold values for the quadtree algorithm to the variance values derived from the error estimation in Section 2.2.1, and retain only polygons containing more than five pixels. This leads to ~500 representative data points for each InSAR image (Table S2). The resulting quadtree images are shown in Fig. 7. Once the interferograms have been resampled we use eq. (2) to build the quadtree covariance matrix E according to the interpolygons distances.

2.3 Coseismic deformation

The coseismic surface deformation we estimate from the campaign and continuous GPS and InSAR observations is shown in Figs 4-6. Most of the surface deformation is concentrated within 10-15 km of the main area of aftershocks, and the amplitudes decay rapidly suggesting that most of the slip occurred above 10 km depth. The largest horizontal coseismic GPS station displacement was recorded at VG22 (258 ± 11 mm towards NW) while the closest CGPS stations (HVER and SELF) moved by 199 ± 4 mm and 201 ± 3 mm towards NW and SE, respectively. A maximum of 100 mm in the direction of LOS was recorded by the ALOS satellite. Smaller displace-

ments were recorded by ENVISAT, which can be explained by the different observation geometry as represented by the LOS unit vectors, where the ALOS satellite is more sensitive to horizontal motion than the ENVISAT.

In the descending interferograms (Fig. 6) we observe a range increase towards north and range decrease southward, which correspond to motion away from the satellite and motion towards the satellite, respectively. Due to the difference in the horizontal component of the LOS unit vectors, the pattern of deformation is reversed in the ascending interferograms. The magnitude of the LOS displacements obtained from the InSAR are consistent with the GPS measurements (Fig. 6).

There are two geodetic benchmarks on top of Kögunarhóll hill that have been observed previously with GPS. The hill is located less than 100 m south of the epicentral location of the Ingólfsfjall earthquake, along the trace of the fault. Two parallel branches of tectonic faulting have been identified here, one on each side of the benchmarks. We observed both sites on Kögunarhóll hill and found that the two points moved apart by 500 mm. The hill sustained significant local deformation and surface cracks were formed, most likely due to amplification of seismic waves radiating from the initial rupture. We therefore do not use GPS data from the Kögunarhóll stations in our modelling.

3 MODELLING

In this section, we explain how we model the coseismic surface deformation observed by campaign and continuous GPS and InSAR. A tomographic study of the epicentral area indicates a strong gradient in the seismic velocities, with the *P*-wave velocity varying from ~4 to ~6 km s^{-1} and the *S*-wave velocity increasing from ~2.3 to ~3.8 km s^{-1}, suggesting an increase in the shear modulus from 12 to 30 GPa in the uppermost 2 km (*Tryggvason et al.* 2002). *Tryggvason et al.* (2002) estimate that the thickness of the brittle part of the crust (i.e. the depth above which 90 per cent of the earthquakes occur) increases from about 5 km on the Reykjanes Peninsula to about 12 km in the eastern part of the SISZ.

In our modelling we account for the depth dependence of the elastic parameters in the crust by using a layered Earth rheology derived by *Dubois et al.* (2008), given in Table 1. We use the software PSCMP/PSGRN (*Wang et al.* 2006) to calculate the surface displacements and the stresses due to slip on rectangular dislocations in a layered half-space. The surface displacements are a non-linear function of the location and geometry of the source, whereas the slip has a linear dependence. We follow a conventional approach of first estimating the dislocation geometry and location assuming constant slip using non-linear optimization. We then use a regularized linear inversion algorithm to solve for variable slip given the optimal dislocation location and geometry estimated in the first step.

Table 1. Elastic parameters.

Depth (km)	Density ρ (kg m^{-3})	Shear modulus μ (GPA)	Poissons's ratio ν
0.0	2306	12.2	0.28
0.6	2512	19	0.28
1.2	2630	25.6	0.28
1.8	2706	30	0.28
2.4	2753	34.3	0.28
3.0	2830	41.3	0.25
8.0	2959	45	0.25
13.0	3322	60	0.30

Notes: Layered earth model for South Iceland initially derived by *Dubois et al.* (2008) based on seismic tomography from *Tryggvason et al.* (2002). The depth is to the top of the layer.

3.1 Uniform slip models from non-linear optimization

Here we estimate the optimal fault locations and geometries, assuming that the faults can be represented as rectangular dislocations with constant slip. The surface displacements have a non-linear relation to the dislocation geometry and location. We use a probabilistic Bayesian approach based on the Metropolis-Hastings algorithm (*Metropolis et al.* 1953), to solve this non-linear problem. Given that each of our model parameter can be expressed by a proposal (or a priori) probability density function (PDF), we can use Bayes' theorem to update the proposal density based on the observed data and the resulting (posterior) PDF is the solution of the inverse problem.

Bayes' theorem states the posterior PDF, $p(\mathbf{m}|\mathbf{d})$, of the model parameters $\mathbf{m}$ given the data $\mathbf{d}$ as

$$p(\mathbf{m}|\mathbf{d}) = \frac{p(\mathbf{m}|\mathbf{d})p(\mathbf{m})}{p(\mathbf{d})} \tag{3}$$

with $p(\mathbf{m})$ the probability of the model parameters and $p(\mathbf{d})$ the probability of the data. The major advantages of the Bayesian approach is that the posterior PDF contains uncertainties as well as interparameter correlations, where other methods only allow us to resolve for one single set of optimal model parameters. In the case of non-linear inversion problems the posterior PDF is difficult to derive analytically, but it can be numerically estimated using a Markov chain Monte Carlo (MCMC) algorithm. We use the Metropolis-Hastings algorithm since it can draw samples from any probability distribution $p(\mathbf{x})$, requiring only that the density can be calculated at $\mathbf{x}$. A popular adaptation of the Metropolis-Hastings algorithm is the Simulated Annealing algorithm which is designed to move faster to the minimum energy state without drawing the complete posterior PDF.

We first need to express the posterior PDF. We assume a priori that the PDF's for the model parameters, $p(\mathbf{m})$, are boxcar functions (i.e. one for a given interval and zero elsewhere), and that the observation errors have a Gaussian distribution with a mean of zero. We use the Bayesian inversion formulation derived by *Fukuda & Johnson* (2008) for the case of multiple data sets with unknown relative weights. The relative weight terms are used to adjust the relative weights of the GPS and InSAR data sets. In our case these estimated terms were close to one indicating appropriate error estimates for the different data sets. Assuming independent errors, the likelihood function we minimize is the product of the likelihoods for each independent data set

Table 2. Uniform slip models.

	Length (km)	Width (km)	Depth (km)	Strike (deg)	Longitude (deg W)	Latitude (deg N)	Strike-slip (m)	χ^2_ν
Kross								
GPS	$6.3^{+1.0}_{-1.5}$	$4.9^{+0.8}_{-3.0}$	$3.5^{+0.7}_{-1.9}$	$3.5^{+0.7}_{-1.9}$	$21.169^{+0.006}_{-0.008}$	$63.951^{+0.008}_{-0.006}$	$1.22^{+0.8}_{-0.4}$	4.6
InSAR	$7.4^{+1.9}_{-2.5}$	$3.3^{+1.2}_{-1.9}$	$2.5^{+0.3}_{-1.1}$	$2.5^{+0.3}_{-1.1}$	$21.175^{+0.002}_{-0.002}$	$63.951^{+0.005}_{-0.003}$	$0.94^{+0.2}_{-0.1}$	6.9
Joint	$8.0^{+1.4}_{-1.2}$	$5.0^{+5.3}_{-2.9}$	$0.3^{+0.1}_{-0.1}$	$2.8^{+1.2}_{-1.5}$	$21.172^{+0.008}_{-0.004}$	$63.961^{+0.003}_{-0.002}$	$0.75^{+0.19}_{-0.01}$	3.5
CGPS	$8.5^{+1.5}_{-3.1}$	$6.5^{+3.4}_{-1.4}$	$0.6^{+2.0}_{-0.6}$	$0.5^{+2.5}_{-0.5}$	$21.175^{+0.009}_{-0.003}$	$63.982^{+0.023}_{-0.015}$	$0.55^{+0.41}_{-0.20}$	3.0
Ingólfsfjall								
GPS	$10.1^{+1.0}_{-1.0}$	$3.9^{+0.5}_{-3.0}$	$2.2^{+0.5}_{-0.5}$	$0.6^{+0.2}_{-0.8}$	$21.075^{+0.009}_{-0.021}$	$63.987^{+0.004}_{-0.012}$	$1.25^{+2.8}_{-0.27}$	4.6
InSAR	$7.8^{+1.4}_{-1.5}$	$5.5^{+1.0}_{-2.1}$	$1.3^{+0.5}_{-0.8}$	$1.1^{+1.3}_{-0.4}$	$21.071^{+0.007}_{-0.018}$	$63.958^{+0.003}_{-0.009}$	$1.8^{+2.1}_{-0.6}$	6.9
Joint	$7.4^{+1.8}_{-1.3}$	$2.0^{+2.2}_{-1.4}$	$1.4^{+0.6}_{-0.6}$	$2.0^{+1.0}_{-1.5}$	$21.070^{+0.002}_{-0.001}$	$63.967^{+0.005}_{-0.004}$	$1.25^{+1.6}_{-0.8}$	3.5
CGPS	$10.1^{+2.1}_{-5.1}$	$5.4^{+4.3}_{-0.4}$	$0.5^{+3.1}_{-0.5}$	$0.0^{+1.7}_{-0.1}$	$21.073^{+0.002}_{-0.011}$	$63.980^{+0.017}_{-0.026}$	$0.79^{+0.2}_{-0.34}$	3.0

Notes: Optimal dislocation model parameters and 1σ confidence intervals assuming two dislocations. The length is measured along strike, and width is the downdip dimension. The depth is measured vertically from the surface down to upper edge of the dislocation. The dip is fixed to 90° (vertical dislocation). The longitude and latitude are the coordinates of the vertical surface projection of the dislocation centre point. The slip is right-lateral strike-slip in metres. The model parameters are given for the three cases considered in this study, that is, using only GPS data, only InSAR data, and from a joint inversion of InSAR and GPS data, as well as those estimated from continuous GPS data by *Hreinsdóttir et al.* (2009) (rows labelled 'CGPS'). The uncertainties estimated on the CGPS models obtained in a different manner than in this study, they are 95 per cent bounds from bootstrap calculations.

$$p(\mathbf{d}_1, \mathbf{d}_2, \ldots, \mathbf{d}_K | \mathbf{m}, \sigma_1^2, \sigma_2^2, \ldots, \sigma_K^2) = \prod_{k=1}^{K} \left\{ (2\pi\sigma_k^2)^{-N_k/2} |\Sigma_k|^{-1/2} \times \exp\left[-\frac{1}{2\sigma_k^2} (\mathbf{d}_k - \hat{\mathbf{d}}_k)^T \Sigma_k^{-1} (\mathbf{d}_k - \hat{\mathbf{d}}_k) \right] \right\} \quad (4)$$

where $\mathbf{d}_k$ are the N_k data of the kth data set, $\mathbf{m}$ the model parameters and $\hat{\mathbf{d}}_k$ the corresponding predicted data, σ_k^2 is an unknown scale factor for the data errors Σ_k of the kth data set. Reintroducing the likelihood function into Bayes' theorem we get the posterior PDF

$$p(\mathbf{m}, \sigma_1^2, \sigma_2^2, \ldots, \sigma_K^2 | \mathbf{m}, \mathbf{d}_1, \mathbf{d}_2, \ldots, \mathbf{d}_K) = \prod_{k=1}^{K} (\sigma_k^2)^{-N_k/2} \exp\left[-\frac{1}{2} \sum_{k=1}^{K} \frac{1}{\sigma_k^2} (\mathbf{d}_k - \hat{\mathbf{d}}_k)^T \Sigma_k^{-1} (\mathbf{d}_k - \hat{\mathbf{d}}_k) \right] \quad (5)$$

Since we can calculate the posterior PDF from eq. (5) for a given set of model parameters $\mathbf{m}$, we can estimate the full PDF with the Metropolis algorithm. The Metropolis algorithm samples the model space using random walk as follows: A candidate model, $\mathbf{m}'$, is generated from the previous step, $\mathbf{m}^{(t)}$, as $\mathbf{m}^{(t)} + \delta(\mathbf{m}_i)$ with $\delta(\mathbf{m}_i)$, a random step according to $p(\mathbf{m})$. $\mathbf{m}'$ is accepted as the new state of the Markov chain only if it satisfies the Metropolis criterion

$$\min\left(1, \frac{p(\mathbf{m}')}{p(\mathbf{m}^{(t)})}\right) > u \sim U(0,1) \quad (6)$$

with u a random number from a uniform distribution over the interval [0, 1]. If the candidate model does not satisfy the Metropolis criterion then the Markov chain remains at the current state, $\mathbf{m}^{(t)}$. After a sufficiently large number of steps, during which the Markov chain converges (also called a 'burn-in' stage) the samples of the Markov chain can be considered as a set of samples drawn from the posterior PDF.

The aftershock locations suggest that more than one fault ruptured in the May 29 sequence. We therefore investigated several different models, increasing the number of dislocations to mimic the aftershock zones. Our analyses indicate that the geodetic data do not require significant slip on more than two main segments, as concluded by *Hreinsdóttir et al.* (2009).

As the data sets span different time intervals, we estimate the optimal model parameters assuming two disloca-

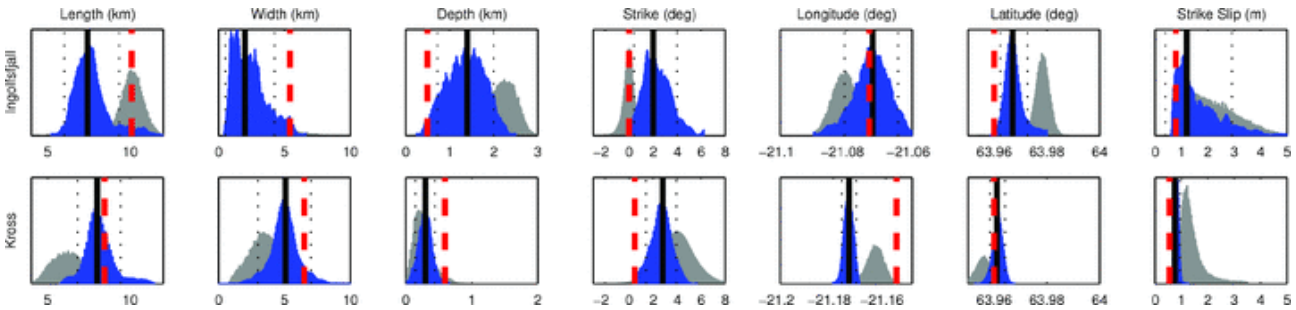

Figure 8. Posterior probability distributions of the uniform slip model parameters using GPS data only (grey) or the joint inversion of GPS and InSAR data (blue). The black lines show the best-fitting model values for the joint inversion, and the dotted lines indicate the 1σ confidence interval. The red dashed lines show the optimal model values estimated by *Hreinsdóttir et al.* (2009) using only the CGPS data.

tion surfaces, first using only the GPS data, then the InSAR data, and finally in a joint inversion using all the data. We select the best model as the maximum likelihood solution (i.e. the solution with the highest probability density). The model parameters are summarized in Table 2 and the posterior PDF's for the parameters are shown in Fig. 8. We found some differences in the estimated model parameters for the three cases. In general, the solutions that include the InSAR data have a narrower range of possible model parameters for the Kross fault, which indicates that the InSAR data provide important constraints on the deformation in the area around the Kross fault. The GPS based inversion suggest that the Ingólfsfjall fault plane extend close to the surface whereas the InSAR data suggest that slip occurred below 2 km depth. Our interpretation is that there is not sufficient near field data to resolve the shallow part of the Ingólfsfjall fault.

To assess how well the models fit the data we calculate the weighted residual sum of squares, $WRSS = \mathbf{r}^T\Sigma^{-1}\mathbf{r}$, where $\mathbf{r}$ is the difference between the observed data and model prediction (i.e. the data residual vector) and Σ^{-1} is the inverse of the data covariance matrix. We report the goodness of fit to the data using $\chi^2_\nu = WRSS/(N-m)$, where N is the number of data and m is the number of model parameters that we estimate. For the uniform slip models N = 2176 and m = 18. Our preferred model is based on the joint inversion of GPS and InSAR data. This model has a lower misfit (χ^2_ν = 3.5) than we find for the optimal models from inversion of only the GPS data (χ^2_ν = 4.6) or the InSAR data (χ^2_ν = 6.9). We suspect that some of the differences in the optimal models are due to inadequate corrections for interseismic signals or rapid post-seismic deformation. However, we argue that these signals are small compared to the coseismic displacements and hence we prefer the model from the joint inversion, as this takes full advantage of the dense spatial coverage of InSAR as well as the 3-D displacement field from the GPS observations. Our best-fitting uniform slip model (from the maximum likelihood estimate) for the Ingólfsfjall fault has 1.2 m of right-lateral strike-slip on an 7.5 km long fault extending from 2 to 4 km. This suggests that most of the slip is concentrated below 2 km. For the Kross fault we estimate a 8 km long fault surface extending from 0.5 to about 5 km depth with 0.75 m of right-lateral strike-slip.

We examine the linear relationship between the model parameters in our study by plotting the correlation matrix (Fig. 9). The absolute value of the correlation coefficient gives a measure of the linear relationship between the model parameters, where a large value (i.e. an absolute value close to one) indicates a strong tradeoff between the parameters and a coefficient of 0 indicates that the vari-

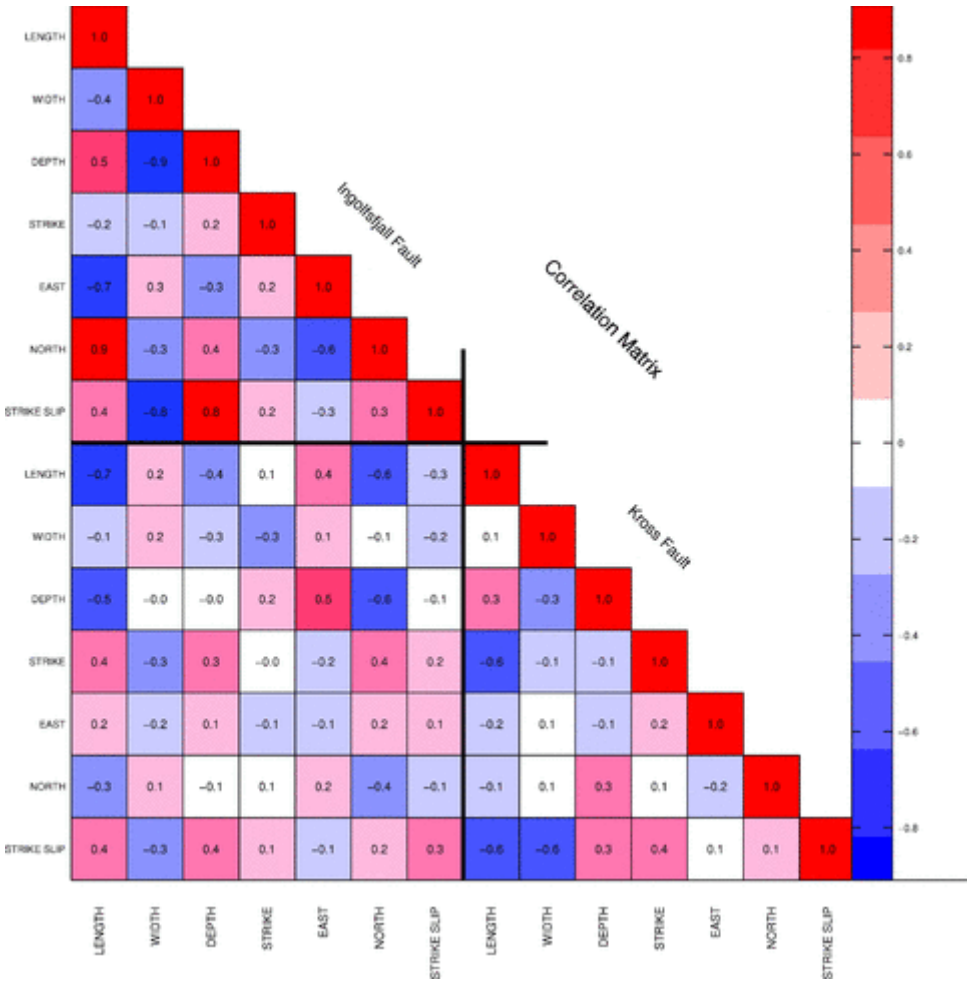

Figure 9. Correlation matrix of the marginal probability distribution of the uniform slip model parameters for the joint inversion. A value of 1 indicates perfect correlation and -1 is perfect anticorrelation.

ables are independent. A negative correlation coefficient suggests an anti-correlation, whereas a positive coefficient represent a positive correlation. As the model parameters have a non-linear relationship to the surface deformation any significant correlation between the resulting model parameters indicates a trade-off that we are not able to resolve with our data set. With a perfect data set (i.e. with adequate spatial sampling and small data errors) one should find all the PDF's to be independent (i.e. all the correlation coefficients are zero). We found a strong correlation (0.87) between the north coordinate and length of the Ingólfsfjall fault, showing that the northern end of the fault is not well constraint. This can be explained by a general decrease of the coherence of the InSAR data on the Ingólfsfjall mountain and the closest GPS benchmark (BURF) is located about 5 km north of the mountain. We also note possible significant anticorrelation between the depth, downdip width, and amount of strike-slip motion, indicating that it is difficult to distinguish between a shallow source with high slip or a wide source with low slip, given our data set. The Kross fault is better resolved, with no correlation coefficient over 0.6. The rather small absolute values of the correlation between the parameters of the two dislocations (maximum value is 0.5) do not indicate substantial trade-off. In particular, the small value for the longitude (E-W location) of the two faults is rather remarkable given the proximity of the ruptures.

3.2 Non-uniform slip models

We estimate the slip distribution on each dislocation using the geometry and locations of our preferred uniform slip models obtained in the previous section. We increase the area of the uniform slip dislocations, so that they extend from the surface to 22 km depth and the length along strike is 25 km. Each rectangular dislocation source is then divided into square patches (0.5 × 0.5 km). In general, the surface displacements are a linear function of the slip. We minimize the weighted misfit (WRSS) between the observed and predicted surface deformation in a least-square sense and assume right-lateral strike-slip only. To regularize the problem, we impose a Laplacian smoothing operator (finite difference L) weighted by a smoothing parameter, κ. Our inversion problem can thus be described as

$$\begin{bmatrix} \mathbf{d}_{gps} \\ \mathbf{d}_{T138} \\ \mathbf{d}_{T367} \\ \mathbf{d}_{T402} \\ \mathbf{d}_{T20} \\ 0 \end{bmatrix} = \begin{bmatrix} G^K_{gps} & G^I_{gps} & 0 & 0 & 0 & 0 \\ G^K_{T138} & G^I_{T138} & 1 & 0 & 0 & 0 \\ G^K_{T367} & G^I_{T367} & 0 & 1 & 0 & 0 \\ G^K_{T402} & G^I_{T402} & 0 & 0 & 1 & 0 \\ G^K_{T20} & G^I_{T20} & 0 & 0 & 0 & 1 \\ \kappa L^K & \kappa L^I & 0 & 0 & 0 & 0 \end{bmatrix} \times \begin{bmatrix} S^K \\ S^I \\ a_{T138} \\ a_{T367} \\ a_{T402} \\ a_{T20} \end{bmatrix} \quad (7)$$

where $\mathbf{d}_{gps}$, $\mathbf{d}_{T138}$, $\mathbf{d}_{T367}$, $\mathbf{d}_{T402}$ and $\mathbf{d}_{T20}$ are the data vectors, G is a matrix that contains Green's functions for the patches on the two dislocation surfaces representing the Kross and the Ingólfsfjall fault, labelled by the superscripts K and I, respectively, S is a vector with the amount of strike-slip on each patch, and a is an arbitrary plane that is estimated to account for possible orbital errors in each interferogram, as noted by the subscripts. The equation system is solved using a fast non-negative least square solver (*Lawson & Hanson* 1974).

The parameter K controls how well the model fits the data versus the roughness of the solution. A model with smoothly varying slip will not fit the data as well as a model that has many localized slip patches but a model with large differences in slip between adjacent patches (i.e. rough slip distribution) is considered physically unrealistic. The usual approach to determine an appropriate smoothing parameter (K) is from a trade-off curve, where one tries to select a value that minimizes both the data misfit and the roughness of the slip model. A more robust approach (*Matthews & Segall* 1993) is to select K using cross-validation sum of squares (CVSS). The CVSS is calculated as the sum of the weighted residuals for a given value of K, in the following manner. An inversion is first performed on a data set omitting one data and the resulting model is then used to calculate the predicted data, for

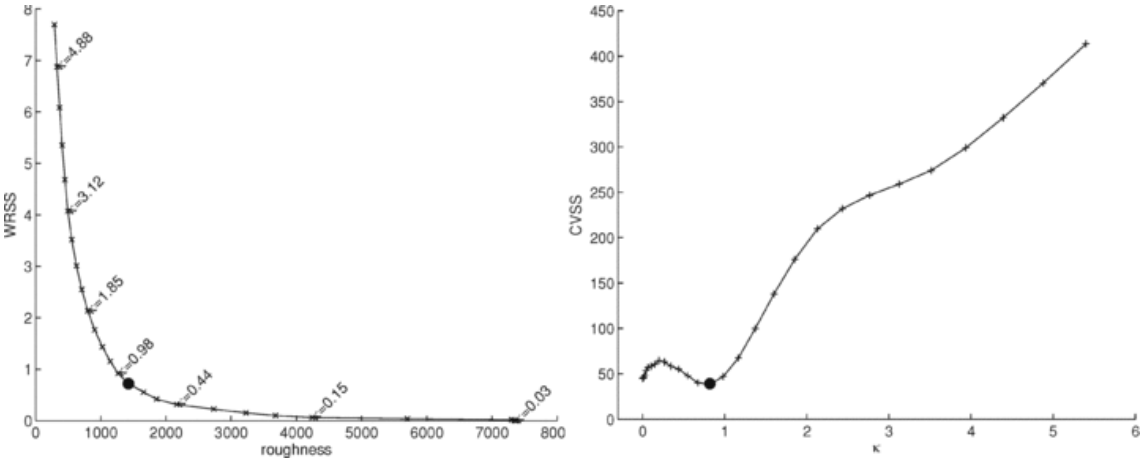

Figure 10. Evaluation of the optimal smoothing parameter (***κ***). Left-hand plot shows the trade-off curve between the weighted residual sum of squares (WRSS) and the model roughness, given the values of ***κ*** (text overlay). Right-hand plot shows the cross validation sum of squares (CVSS) versus ***κ***. The dot indicates the preferred value of ***κ*** = 0.8 on both graphs.

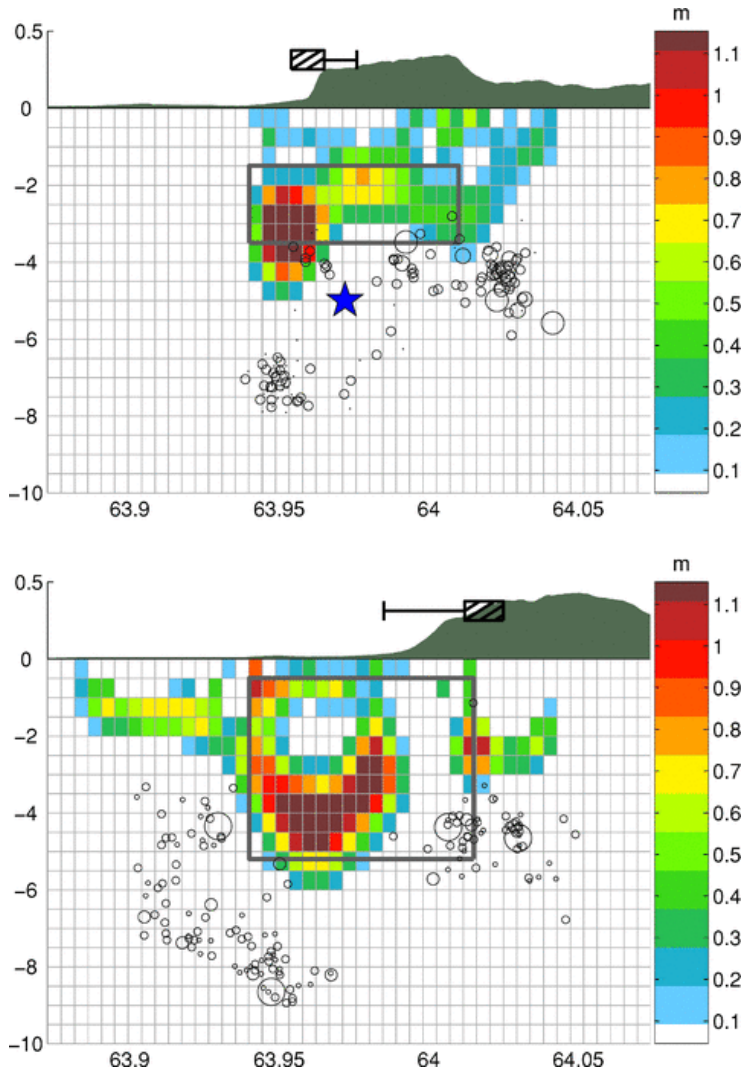

Figure 11. Variable slip model for the Ingólfsfjall fault (top panel) and the Kross fault (bottom panel). The amount of right-lateral strike-slip is shown with the colour scale (same for both figures). The black circles denote aftershocks recorded by the SIL network between 2008 June 2 and July 10. The locations of the constant slip models are shown with a grey outline. The black boxes indicate locations of mapped surface fractures, and the black lines show areas where the mapped fractures may be secondary features, rather than surface expressions of the 2008 May events.

the data that was not included in the inversion. The difference between the data and the model prediction weighted by the data error is the weighted residual. This procedure is repeated for each datapoint and a range of K and the minimum CVSS indicates the optimal smoothing value, given the data. We select a smoothing value of K = 0.8 which is optimal from both the trade-off curve and the CVSS calculation (Fig. 10).

We calculate the resolution kernel of the inverse problem for the different data sets define by *Tarantola* (2005) as

$$R = G^T(GG^T)^{-1}G. \quad (8)$$

The resolution (dimensionless) is 1 in the well-resolved areas and 0 in unresolved areas. A plot of the resolution kernel (Fig. S1) shows that we can resolve the slip distribution down to ~8 km on the two fault planes for a joint inversion of GPS and InSAR data. The resolution is smoothly decreasing with depth indicating that we should not get any artefacts in the slip distribution due to the geometry of our observation network.

The estimated slip distributions are shown in Fig. 11 and the data residuals in Fig. 12. Most of the slip on the Kross fault is focused in an area that is approximately 5 km long and extends from 3 to 6 km depth with a maximum motion of 1.4 m. A second, smaller slip maximum is located further north, above a cluster of aftershocks. The slip model we obtain for the Ingólfsfjall event suggests smaller area of slip but a larger slip amplitude than on the Kross fault. The slip is concentrated in a 4 × 2 km area centred at approximately 3 km depth, and decreases smoothly from a maximum of 1.9 m to less than 0.5 m over a distance of 8 km towards north.

The geodetic moment release of our model for the Kross fault is $M_0 = \mu As = 8.65 \times 10^{17}$ Nm, where A is the fault area, s is the slip, and μ is given Table 1. This geodetic moment corresponds to a seismic moment magnitude of M_w5.9, using $M_w = 2/3 \log_{10} M_0 - 6.03$. For the Ingólfsfjall fault we estimate a geodetic moment of 5.97 × 10^{17} Nm, corresponding to a moment magnitude of M_w5.8. Our models therefore give a cumulative geodetic moment for the doublet of M_0 = 1.46 × 10^{18} Nm, equiva-

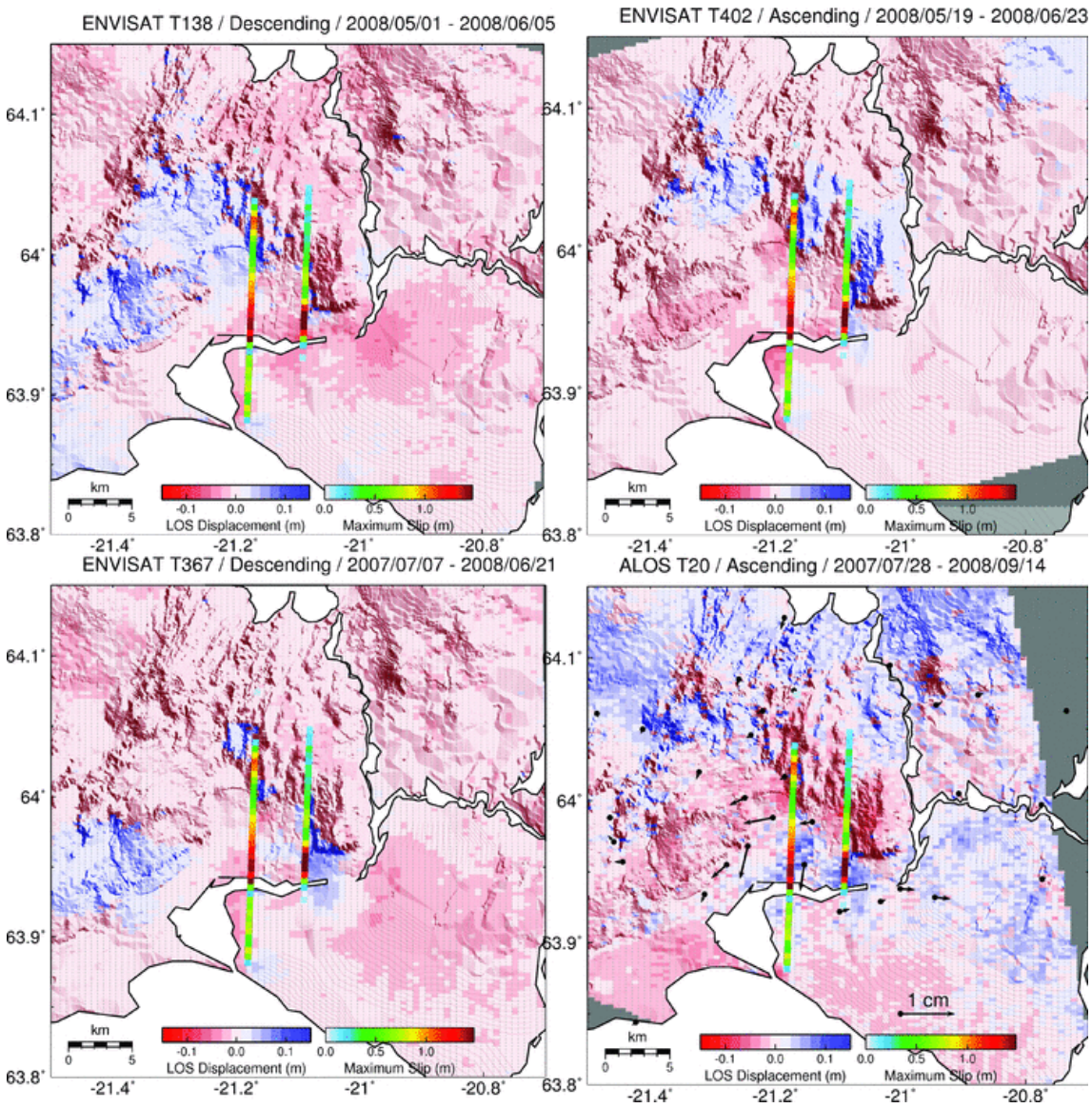

Figure 12. InSAR residuals from the non-uniform slip model are shown with the colour scale and the GPS residuals with arrows. The slip models are indicated by a bold line showing the maximum slip value at depth.

lent to a single event with a moment magnitude of M_w6.1.

3.3 Coseismic static Coulomb failure stress change

We calculate the static Coulomb stress changes predicted by our variable slip models using the layered Earth rheology, to examine possible stress triggering of the second event and how stress changes predicted from our model agree with aftershock locations.

The change in the static Coulomb failure stress change (ΔCFS) is estimated from (e.g. *Harris* 1998)

$$\Delta CFS = \Delta\tau_S + \mu_f \left(\Delta\sigma_n - \frac{B}{3}\Delta\sigma_{kk}\right), \quad (9)$$

where $\Delta\tau_S$ is the change in shear stress resolved in the slip direction of a fault that may fail in a subsequent event, $\Delta\sigma_n$ is the change in normal stress on the receiver faults, and $\Delta\sigma_{kk}$ is the change in volumetric stress. Here, μ_f is the coefficient of friction (we assume μ_f = 0.75) and B is Skempton's coefficient (B = 0.5). The stress change depends on the location and orientation of the receiver faults. Here, the AC FS is calculated on N-S right-lateral strike-slip faults at 5 km depth. A positive ΔCFS implies an increase in the Coulomb failure stress, that may promote failure on secondary faults. Our models predict positive static Coulomb stress changes following the Ingólfsfjall event at the location of the maximum slip on the Kross fault model (Fig. 13a). This suggests that the coseismic stress changes caused by the Ingólfsfjall event promoted failure on the Kross fault. Analysis of high-rate (1 Hz) CGPS data indicate that slip on the second fault initiated within 3 s of the initial main shock (*Hreinsdóttir et al.* 2009). Therefore, we cannot preclude dynamic stress triggering of the second event from the geodetic data. The positive Coulomb stress changes associated with the two main events correlate spatially with aftershock locations recorded by the SIL seismic network after the main shocks (Fig. 13b). Furthermore, our models

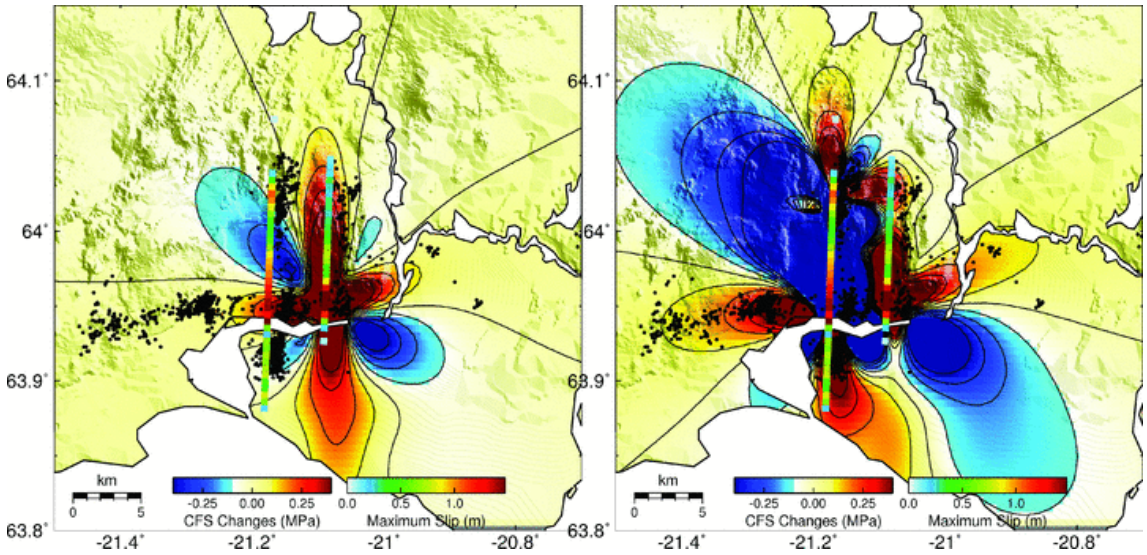

Figure 13. Static Coulomb failure stress changes for N-S right-lateral strike-slip faults at 5 km depth. The contours are 0.1 MPa. The left-hand panel shows the $\Delta \boldsymbol{CFS}$ calculated from the variable slip model for the Ingólfsfjall event and the right-hand panel is the total $\Delta \boldsymbol{CFS}$ predicted from the Ingólfsfjall and Kross models. The thick lines represent the surface projections of the dislocation models, where the colour indicates the maximum slip at depth. The black dots show the locations of aftershock recorded by the SIL network from 2008 June 2 to July 10.

indicate an increase in the Coulomb failure stress in the area west of the Kross fault and east of the Ingólfsfjall fault. Very few aftershocks were located on the Ingólfsfjall fault, while intense activity has continued on the southern part of the Kross fault.

4 DISCUSSION

4.1 Fault models

Our modelling shows that the coseismic deformation observed by GPS and InSAR can be explained by right-lateral motion on two parallel N-S striking faults, spaced about 5 km apart, in agreement with a previous study using only CGPS data (*Hreinsdóttir et al.* 2009). We find that the Kross fault is located slightly further west than in the models by *Hreinsdóttir et al.* (2009), based on data from two GPS stations located near the trace of the Kross fault (AUDS and GLJU), as well as pixels in the descending InSAR image located in the area between the two faults. We also note that the Ingólfsfjall rupture determined from the geodetic data lies to the west of where most of the aftershocks are located (e.g. Fig. 4), in agreement with field observations of surface ruptures in the epicentral area. Preliminary results from a local seismic network deployed after the May 29 earthquakes indicate that the aftershock locations from the SIL network may be ~500 m too far east, due to variations in the seismic structure in the area that is not included in the SIL seismic model (*B. Brandsdóttir* 2009, personal communication).

Our best-fitting uniform slip model for the Ingólfsfjall fault suggests that most of the slip there occurred below 2 km which is deeper than the uniform slip model estimated by *Hreinsdóttir et al.* (2009). In general, we find higher slip over smaller fault surfaces, than *Hreinsdóttir et al.* (2009). Our variable slip models can explain 95 per cent of the data variance. The geodetic models suggest that the slip on the Kross fault was concentrated in two main patches, similar to the features found in the slip models estimated from CGPS data by *Hreinsdóttir et al.* (2009). Our study shows that most of the slip occurred north of the Ölfusá river, which is consistent with locations of surface fractures (Fig. 11). The variable slip model we obtain for the Ingólfsfjall event has less slip than on the Kross fault. The main patch in our model is located further south than in the CGPS model by *Hreinsdóttir et al.* (2009). The reason for this is most likely that there are only two continuous GPS stations located near the southern end of the Ingólfsfjall fault, whereas our data set includes several additional campaign GPS and InSAR data in the near-field area (Fig. 4). In particular, the GPS campaign stations LJOS, BURF, SELH and ONDV located 5-8 km from the northern part of the Ingólfsfjall fault show smaller coseismic displacements than the CGPS station SELF (in Selfoss), indicating that there was less slip on the northern part of the fault than on the southern part. The decrease of coseismic displacement eastward from the southern end of the Ingólfsfjall fault (i.e. at SELF, ISMA, HAAL) also indicates that most of the slip occurred at shallow depth on the southern part. The main slip on the Kross fault is roughly at the same location in both geodetic studies, confirming that the differences between the slip on the Ingólfsfjall fault estimated by *Hreinsdóttir et al.* (2009) and in this study are primarily due to an increase in the model resolution when including the GPS campaign data and the InSAR images.

We also performed a joint inversion of the GPS and InSAR data assuming a half-space rheology (with ν = 0.28). From a comparison between this and our optimal model, we conclude that the layered earth model produces lower slip magnitudes (0.25-0.5 m) and shallower slip (1-2 km) than the half-space model. *Dubois et al.* (2008), however, found more slip at depth when using a layered earth model to estimate the variable slip for the 2000 June events. In general, the slip models depend on the available

Table 3. Earthquakes in the SISZ.

Date	Lat.	Lon.	Magnitude	District/location
1630/02/21	64.00	20.21	7	Land, Minnivellir
1633/–/–	–	–	–	Ölfus
1706/04/20	63.90	21.20	6.0	Ölfus, Hverageröi
1732/09/07	64.00	20.04	6.7	Land, Leirubakki?
1734/03/21	63.90	20.83	6.8	Flói, Litlu-Reykir?
1766/09/09	63.90	21.16	6.0	Ölfus, Gljúfur Kross
1784/08/14	63.90	20.47	7.1	Holt - Gíslholtsvatn
1784/08/16	63.90	20.95	6.7	Flói - Laugardælir
1829/02/21	63.90	20.0	6.0	Rangárvellir - Hekla
1896/08/26	64.00	20.13	6.9	Skarðsfjall - Fellsmúli
1896/08/27	64.00	20.26	6.7	Flagbjarnarh. -Lækjarbotnar
1896/09/05	63.90	21.04	6.0	Selfoss – Ingólfsfjall
1896/09/05	64.00	20.57	6.5	Skeið - Arakot -Borgarkot
1896/09/06	63.90	21.20	6.0	Ölfus - Hverageröi
1912/05/06	63.90	19.95	7.0	Selsund - Galtalækur
2000/06/17	63.973	20.367	6.6(6.5)	Holt, Skammbeinsstaðir
2000/06/21	63.972	20.711	6.5(6.4)	Flói, Grímsnes, Hestvatn
2008/05/29	63.972	21.072	6.3(5.8,5.9)	Ölfus doublet (Ingólfsfjall, Kross)

Notes: Moderate size ($M > 6$) earthquakes in SISZ since 1600. The magnitudes of the events we report are M_S and the moment magnitudes for events in 2000 and 2008, estimated from geodetic studies are given in parenthesis.

data (which affects the model resolution), the earth model, the choice of the smoothing imposed on the model and the depth of the slip source.

The geodetic moments estimated from the variable slip models indicate that the initial event on the Ingólfsfjall fault was slightly smaller than the triggered rupture on the Kross fault. The magnitude and geodetic moment estimates using the depth dependent rigidity are, however, very similar to the half-space models (the difference in M_w is less than 0.02). Using a layered earth model rather than an elastic half-space thus affects the slip magnitude and depth in the variable slip model, but is unlikely to cause a shift in the latitude of the slip estimates. We note that aftershocks appear to cluster adjacent to the regions of coseismic slip on both faults (Fig. 11). In general, aftershocks are expected to occur in areas of large stress changes on and off the ends of the fault surface, as reported in many studies (e.g. *Massonnet & Feigl* 1993; *Cohee & Beroza* 1994; *Pedersen et al.* 2003; *Johanson et al.* 2006). The events in the 2008 May sequence are smaller than the 2000 June, which ruptured 10-15 km long faults with up to 2–3 m of slip, located above 10 km depth (*Pedersen et al.* 2003). The decrease in earthquake size is consistent with thinning of the brittle part of the crust from about 12 km in the east to ~5 km in the west (e.g. *Tryggvason et al.* 2002; *Árnadóttir et al.* 2006). As for the 2000 June main shocks, we find a high ratio of slip to fault length indicating high stress drop in these earthquakes. This has also been noted for earlier events in the SISZ and interpreted as evidence for the SISZ being a young and immature fault zone (*Bjarnason et al.* 1993a).

4.2 The 2000–2008 earthquake sequence in a tectonic context

The SISZ accommodates 18-20 mm yr^{-1} of relative plate motion across an approximately 20 km wide N-S zone. The strain accumulated during a century could therefore be released as ~2 m of coseismic slip along the E-W length of the zone. The May 29 events follow the faulting pattern observed in earlier events, which limits the seismic hazard to magnitude 6-7 earthquakes rupturing 10-20 km long N-S faults instead of the ~80 km E-W transform along the SISZ. To model the earthquake cycle in the SISZ we assume that moment accumulated by deep shear in the SISZ is released by brittle failure in the crust. *Sigmundsson et al.* (1995) showed that the moment release by rupture of many closely spaced, short N-S faults is equivalent to that released by a single E-W transform fault for the SISZ. We therefore calculate the geodetic moment built up by plate motion using an average constant locking depth ranging between the estimates for the eastern and western part of the SISZ (12 ± 2 km) (e.g. *Tryggvason et al.* 2002; *Árnadóttir et al.* 2006), and a constant rate of slip (19 ± 1 mm yr^{-1}) in an 80 km E–W zone. We compare this moment accumulation to the moment released in moderate size ($M > 6$) earthquakes. A list of significant earthquakes in the SISZ since 1600 AD is given in Table 3. The magnitudes of events are after *Stefánsson & Halldórsson* (1988) and are based on the size of destruction areas of the historical earthquakes as published by *Björnsson & Einarsson* (1981). The identification of the source faults of these earthquakes is given by *Einarsson et al.* (1981), *Einarsson & Eiríksson* (1982), *Bjarnason et al.* (1993a) and *Khodayar et al.* (2007) and is based on field mapping of surface ruptures and historical documents compiled by *Thoroddsen* (1899, 1925).

The geodetic moment accumulation and seismic moment release from this model is shown in Fig. 14. The start of the loading history is arbitrarily adjusted so that the 1912 event produces a complete release of the accumulated moment. Fig. 14 shows that the model is consistent with an almost complete release of the accumulated moment during 1732-1784, and in 1630. During a seismic cycle in the SISZ the moment is built up by plate motion and completely released by earthquakes in the whole zone, whether they occur in one or more earthquake sequences and single events (Fig. 14). This indicates that the seismic cycle in the SISZ is 130-150 yr, whereas the time between historical

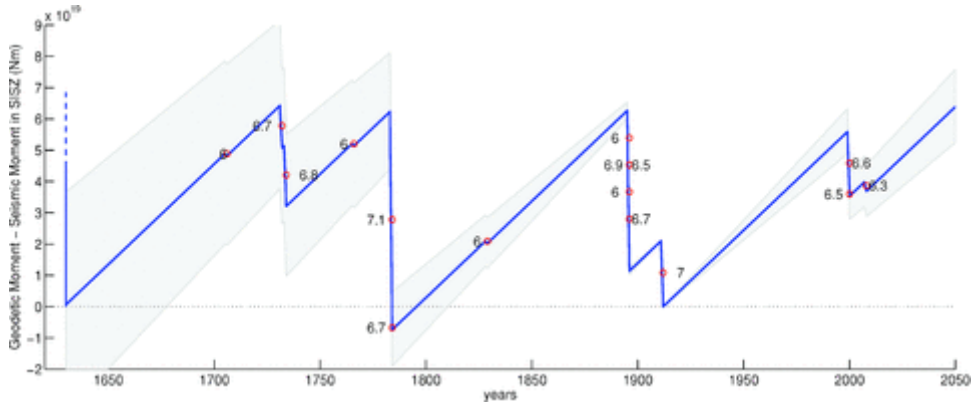

Figure 14. Model of the seismic cycle in the SISZ as a function of time since 1600. The interseismic periods are represented by the accumulation of geodetic moment in the SISZ, as explained in the text. The seismic moment released in moderate size events in the SISZ (red circles) is calculated for the events listed in Table 3. The grey area shows the range of possible values assuming a ±0.05 uncertainty in the seismic magnitude estimates and ±2 km in the locking depth.

earthquake sequences in the SISZ varies between 45 and 112 yr with the individual earthquake sequences lasting up to 2 yr (*Einarsson et al.* 1981). For example, the 1732 and 1734 earthquakes are considered to be an earthquake sequence, as are the two 1784 magnitude 7.1 and 6.7 events that occurred in a span of 2 d, whereas the 1912 event is often given as an example of a single event, not considered part of the 1896 earthquake sequence *(Einarsson et al.* 1981). We see that it took 16 yr (1896–1912) to release the moment accumulated by ~100 yr of plate motion, whereas the accumulated moment was released over a much longer time interval (1732–1784) in two main earthquake sequences during the preceding earthquake cycle. Whether one considers the 2000 June and 2008 May events as the same sequence or two separate sequences, it is clear from Fig. 14 that the moment release in the 2000–2008 events is less than in the 1896 sequence (after five M_S = 6-6.9 events). This indicates that there is still potential for a moment release equivalent to a M_w = 7 event in South Iceland. We note, however, that the accuracy of the seismic history is critical for this analysis and a change of ±0.05 in the estimated magnitudes can lead to different scenarios. Furthermore, this analysis does not identify what segment of the SISZ will rupture in the next moderate size event(s). The 2000-2008 June sequence has now reached the western part of the SISZ and more detailed studies, including a plate boundary model that accounts for the crustal thickening and stress changes due to post-seismic deformation is needed to address whether the activity is likely continue with similar size or larger events in the eastern part of the SISZ or with moderate size earthquakes in the central and/or western part of the region.

5 CONCLUSIONS

We present models of the faults that ruptured in the 2008 May 29 earthquake doublet in the South Iceland Seismic Zone. We use a joint inversion of InSAR and GPS data to estimate the geometry, location and distribution of the slip on the fault planes. In our models we account for the depth dependence of the elastic parameters in the Icelandic crust. We interpret the May 29 events as earthquakes rupturing two vertical N-S right-lateral strike-slip faults. The first rupture occurred along the Ingólfsfjall fault and our models indicate localized and shallow slip. The second event was triggered on the Kross fault. The depth extent of the ruptures are shallower than found in models for the 2000 June events, which is consistent with the brittle part of the crust thickening towards the east along the SISZ. Aftershock locations correlate spatially with both static Coulomb failure stress changes and the areas of high coseismic slip is adjacent to concentrations of aftershocks. Our models have geodetic moments of 8.65×10^{17} and 5.97×10^{17} Nm, corresponding to moment magnitudes of M_w = 5.9 and 5.8 for the Kross and the Ingólfsfjall faults, respectively. The June 2000-2008 earthquake sequence has only released about half of the moment accumulated by plate motion since the last major earthquake sequence in the SISZ (1896-1912). It is therefore likely that the sequence will continue with moderate size earthquakes in the SISZ in the coming years.

ACKNOWLEDGMENTS

We thank UNAVCO, the National Land Survey of Iceland, the Icelandic Road Authority, and Landsvirkjun for lending us GPS equipment and assisting with the GPS post-earthquake fieldwork in 2008. Comments from Kurt Feigl and one anonymous reviewer helped us improve the text. Ingvar Magnússon at ISOR provided GPS data from 2007. Pierre Dublanchet from ENS helped with the GPS measurements in 2008. We thank Bryndís Brandsdóttir for discussions and sharing of preliminary results from her seismic studies and Sigurjón Jónsson for the InSAR processing discussions. This work was funded by grants from the Icelandic Research Council, United State National Science Foundation (NSF grants number EAR0711446 and EAR-0711456), the University of Arizona, Pennsylvania State University and the University of Iceland Research Fund.

REFERENCES

Antonioli, A., Belardinelli, M., Bizzarri, A. & Vogfjörd, K.S., 2006. Evidence of instantaneous dynamic triggering during the seismic sequence of year 2000 in south Iceland, *J. Geophys. Res.*, **111**, B03302, doi:10.1029/2005JB003935.

Árnadóttir, T., Hreinsdóttir, S., Gudmundsson, G., Einarsson, P., Heinert, M. & Völksen, C., 2001. Crustal deformation measured by GPS in

the South Iceland Seismic Zone due to two large earthquakes in June 2000, *Geophys. Res. Lett.*, **28**, 4031–4033.

Árnadóttir, T., Jónsson, S., Pedersen, R. & Gudmundsson, G.B., 2003. Coulomb stress changes in the South Iceland Seismic Zone due to two large earthquakes in June 2000, *Geophys. Res. Lett.*, **30**(5), 1205, doi:10.1029/2002GL016495.

Árnadóttir, T., Geirsson, H. & Einarsson, P., 2004. Coseismic stress changes and crustal deformation on the Reykjanes Peninsula due to triggered earthquakes on 17 June 2000, *J. Geophys. Res.*, **109**, B09307, doi:10.1029/2004JB003130.

Árnadóttir, T., Jiang, W., Feigl, K.L., Geirsson, H. & Sturkell, E., 2006. Kinematic models of plate boundary deformation in southwest Iceland derived from GPS observations, *J. Geophys. Res.*, **111**, B07402, doi:10.1029/2005JB003907.

Bellou, M., Bergerat, F., Angelier, J. & Homberg, C., 2005. Geometry and segmentation mechanisms of the surfaces traces associated with the 1912 Selsund earthquake, southern Iceland, *Tectonophysics*, **404**, 133–149.

Bjarnason, I., Cowie, P., Anders, M.H., Seeber, L. & Scholz, C.H., 1993a. The 1912 Iceland earthquake rupture: growth and development of a nascent transform system, *Bull. Seism. Soc. Am.*, **83**, 416–435.

Bjarnason, I., Menke, W., Flóvenz, ó.G. & Caress, D., 1993b. Tomographic image of the mid-Atlantic plate boundary in southwestern Iceland, *J. Geophys. Res.*, **98**, 6607–6622.

Björnsson, S. & Einarsson, P., 1981. Jarðskjálftar (Earthquakes, in Icelandic), in *Náttúra Íslands*, pp. 121–155, eds Þórarinsdóttir, H. & Steinpórsson, S., Almenna Bókafélagið, Reykjavík.

Clifton, A.E. & Einarsson, P., 2005. Styles of surface rupture analysis accompanying the June 17 and 21, 2000 earthquakes in the South Iceland Seismic Zone, *Tectonophysics*, **396**, 141–159.

Clifton, A.E., Pagli, C., Jónsdóttir, J.F., Eythórsdóttir, K. & Vogfjörd, K., 2003. Surface effects of triggered fault slip on Reykjanes Peninsula, SW Iceland, *Tectonophysics*, **369**, 145–154.

Cohee, B.P. & Beroza, G.C., 1994. Slip distribution of the 1992 Landers earthquake and its implications for earthquake source mechanics, *Bull. Seism. Soc. Am.*, **84**, 692–712.

Dach, R., Hugentobler, U., Fridez, P. & Meindl, M., 2007. Bernese GPS software version 5.0, Technical report, Astronomical Institute, University of Bern, Bern, Switzerland.

Decriem, J. et al., 2008. Unraveling faulting in a complex earthquake sequence in the South Iceland Seismic Zone, in *EOS, Trans. Am. Geophys. Un.*, **89**(53), Fall Meet. Suppl., Abstract T41A-1926, AGU.

DeMets, C.G., Gordon, R., Argus, D.F. & Stein, S., 1994. Effect of recent revisions to the geomagnetic reversal time scale on estimates of current plate motions, *Geophys. Res. Lett.*, **21**, 2191– 2194.

Dubois, L., Feigl, K.L., Komatitsch, D., Árnadóttir, T. & Sigmundsson, F., 2008. Three-dimensional mechanical models for the June 2000 earthquake sequence in the south Iceland seismic zone, *Tectonophysics*, **457**, 12–29.

Einarsson, P., 1991. Earthquakes and present-day tectonism in Iceland, *Tectonophysics*, **189**, 261–279.

Einarsson, P. & Eiríksson, J., 1982. Earthquake fractures in the districts Land and Rangárvellir in the South Iceland Seismic Zone, *Jökull*, **32**, 113–120.

Einarsson, P., Björnsson, S., Foulger, G., Stefánsson, R. & Skaftadóttir, T., 1981. Seismicity pattern in the South Iceland Seismic Zone, in *Earthquake Prediction - An International Review*, Vol. 4, pp. 141–151, eds Simpson, D.W. & Richards, P.G., AGU, Washington DC.

Foulger, G.R., Bilham, R., Morgan, W.J. & Einarsson, P., 1987. The Icelandic GPS geodetic field campaign 1986, *EOS, Trans. Am. geophys. Un.*, **68**, 1809.

Fukuda, J. & Johnson, K.M., 2008. A fully Bayesian inversion for spatial distribution of fault slip with objective smoothing, *Bull. Seism. Soc. Am.*, **3**, 1128–1146.

Geirsson, H., Árnadóttir, T., Völksen, C., Jiang, W., Sturkell, E., Villemin, T., Einarsson, P. & Sigmundsson, F., 2006. Current plate movements across the Mid-Atlantic ridge determined from 5 years of continuous GPS measurements in Iceland, *J. Geophys. Res.*, **111**, B09407, doi:10.1029/2005JB003717.

Halldórsson, B. & Sigbjörnsson, R., 2009. The M_w6.3 Ölfus earthquake at 15:45 UTC on May 29 2008 in South Iceland: ICEARRAY strong-motion recordings, *Soil Dyn. Earthq. Eng.*, **29**, 1073–1083, doi:10.1016/j.soildyn.2008.12.006.

Harris, R.A., 1998. Introduction to special section: stress triggers, stress shadows, and implications for seismic hazard, *J. Geophys. Res.*, **103**, 24 347–24 358.

Herring, T.A., King, R.W. & McClusky, S.C., 2006. GLOBK reference manual, Global Kalman filter VLBI and GPS analysis program, release 10.3, Technical report, *Mass. Inst. Technol.*, Cambridge, MA, USA.

Hjaltadóttir, S., 2009. Use of relatively located microearthquakes to map fault patterns and estimate the thickness of the brittle crust in Southwest Iceland, *Master's thesis*, Faculty of Earth Sciences, University of Iceland, Reykjavík, Iceland.

Hooper, A., Segall, P., Johnson, K. & Zebker, H.A., 2007. Persistent scatterer InSAR for crustal deformation analysis, with application to Volcan Alcedo, Galapagos, *J. Geophys. Res.*, **112**, B07407, doi:10.1029/2006JB004763.

Hooper, A., 2009. A statistical-cost approach to unwrapping the phase of InSAR time series, in *Proceedings of ESA FRINGE Workshop, Frescati, Italy, November 30–December 4, 2009*, in press.

Hreinsdóttir, S., Einarsson, P. & Sigmundsson, F., 2001. Crustal deformation at the oblique spreading Reykjanes Peninsula, SW Iceland: GPS measurements from 1993 to 1998, *J. Geophys. Res.*, 106, 13 803–13 816.

Hreinsdóttir, S., Árnadóttir, T., Decriem, J., Geirsson, H., Tryggvason, A., Bennett, R.A. & LaFemina, P., 2009. A complex earthquake sequence captured by the continuous GPS network in SW Iceland, *Geophys. Res. Lett.*, **36**, L12309.

Johanson, I., Fielding, E.J., Rolandone, F. & Bürgmann, R., 2006. Coseismic and postseismic slip of the 2004 Parkfield earthquake from space-geodetic data, *Bull. Seism. Soc. Am.*, **96**, 5269–5282.

Jónsson, S., 2008. Importance of post-seismic viscous relaxation in southern Iceland, *Nature*, **1**, 136–139.

Jónsson, S., Zebker, H.A., Segall, P. & Amelung, F., 2002. Fault slip distribution of the 1999 M_w7.2 Hector Mine earthquake, California, estimated from satellite radar and GPS measurements, *Bull. Seism. Soc. Am.*, **92**, 1377–1389.

Jónsson, S., Segall, P., Pedersen, R. & Björnsson, G., 2003. Post-earthquake ground movements correlated to pore-pressure transients, *Nature*, **424**, 179–183.

Keiding, M., Árnadóttir, T., Sturkell, E., Geirsson, H. & Lund, B., 2008. Strain accumulation along an oblique plate boundary: the Reykjanes Peninsula, southwest Iceland, *Geophys. J. Int.*, **172**(1), 861–872, doi:10.1111/j.1365-246X.2007.03655.x.

Khodayar, M., Franzson, H., Einarsson, P. & Björnsson, S., 2007. Hvammsvirkjun. Geological investigation of Skarðsfjall in the South Iceland Seismic Zone., Technical report. ÍSOR-2007/017, LV-2007/065, Íslenskar Orkurannsóknir, Reykjavík, Iceland.

LaFemina, P.C., Dixon, T.H., Malservisi, R., Árnadóttir, T., Sturkell, E., Sigmundsson, F. & Einarsson, P., 2005. Geodetic GPS measurements in south Iceland: strain accumulation and partitioning in a propagating ridge system, *J. Geophys. Res.*, **110**, B11405, doi:10.1029/2005JB003675.

Lawson, C. & Hanson, R., 1974. Solving Least Squares Problems, Prentice Hall, Englewood Cliffs.

Lindman, M., 2009. Physics of aftershocks in the South Iceland Seismic Zone, *PhD thesis*, Faculty of Science and Technology, Uppsala University, Uppsala, Sweden.

Massonnet, D. & Feigl, K.L., 1993. Radar interferometry and its application to changes in the earth's surface, *Rev. Geophys.*, **36**(4), 441–550.

Matthews, M. & Segall, P., 1993. Statistical inversion of crustal deformation data and estimation of the depth distribution of slip in the 1906 earthquake, *J. Geophys. Res.*, **98**, 12 153–12 163.

McClusky, S. et al., 2000. Global Positioning System constraints on plate kinematics and dynamics in the eastern Mediterranean and Caucasus, *J. Geophys. Res.*, **105**(B3), 5695–5720.

Metropolis, N., Rosenbluth, A., Rosenbluth, M., Teller, A. & Teller, E., 1953. Equations of State Calculations by Fast Computing Machines, *J. Chem. Phys.*, **21**, 1087–1091.

Pagli, C., Pedersen, R., Sigmundsson, F. & Feigl, K.L., 2003. Triggered seismicity on June 17, 2000 on Reykjanes Peninsula, SW-Iceland captured by radar interferometry, *Geophys. Res. Lett.*, **30**(6), 1273, doi:10.1029/2002GL015310.

Pedersen, R., Sigmundsson, F., Feigl, K.L. & Árnadóttir, T., 2001. Coseismic interferograms of two M_S = 6.6 earthquakes in the South Iceland Seismic Zone, June 2000, *Geophys. Res. Lett.*, **28**, 3341–3344.

Pedersen, R., Jónsson, S., Árnadóttir, T., Sigmundsson, F. & Feigl, K.L., 2003. Fault slip distribution of two M_w = 6.5 earthquakes in South Iceland estimated from joint inversion of InSAR and GPS measurements, *Earth planet Sci. Lett.*, **213**, 487–502.

Sella, G.F., Dixon, T.H. & Mao, A., 2002. REVEL: a model for recent plate velocities from space geodesy, *J. Geophys. Res.*, **107**, ETG 11-1-31, doi:10.1029/2000JB000033.

Sigmundsson, F., Einarsson, P., Bilham, R. & Sturkell, E., 1995. Rift-

transform kinematics in south Iceland: deformation from Global Positioning System measurements, 1986 and 1992, *J. Geophys. Res.*, **100**, 6235–6248.
Stefánsson, R. & Halldórsson, P., 1988. Strain release and strain build-up in the south Iceland seismic zone, *Tectonophysics*, **152**, 267–276.
Stefánsson, R. et al., 1993. Earthquake Prediction Research in the South Iceland Seismic Zone and the SIL Project, *Bull. Seism. Soc. Am.*, **83**(3), 696–716.
Sudhaus, H. & Jónsson, S., 2008. Improved source modelling through combined use of InSAR and GPS under consideration of correlated data errors: application to the June 2000 Kleifarvatn earthquake, Iceland, *Geophys. J. Int.*, **176**, 389–404.
Tarantola, A., 2005. *Inverse Problem Theory and Methods for Parameter Estimation*, SIAM, Philadelphia.
Thoroddsen, T., 1899. Jarðskjálftar á Suðurlandi (Earthquakes in South Iceland, in Icelandic), *Hið íslenska bókmenntafélag (The Icelandic Literary Society)*, p. 269.
Thoroddsen, T., 1925. Die Geschichte der Isländischen Vulkane (The history of Icelandic volcanoes, in German), *D. Kgl. Danske Vidensk. Selsk. Skrifter*, p. 458 and 5 pl.
Tryggvason, A., Rögnvaldsson, S.T. & Flóvenz, ó.G., 2002. Threedimensional imaging of the P- and S-wave velocity structure and earthquake locations beneath Southwest Iceland, *Geophys. J. Int.*, **151**, 848–866.
Vogfjörd, K.S., 2003. Triggered seismicity in SW Iceland after the June 17, M_w = 6.5 earthquake in the South Iceland Seismic Zone: the first five minutes, in *Geophys. Res. Abs*., EAE03-A-11251, Vol. 5, European Geosciences Union.
Wang, R., Lorenzo, F. & Roth, F., 2006. PSGRN/PSCMP - a new code for calculating co- and post-seismic deformation, geoid and gravity changes based on viscoelastic-gravitational dislocation theory, *Comput. Geosci.*, **32**, 527–541.

SUPPORTING INFORMATION

Additional Supporting Information may be found in the online version of this article:

Figure S1. Resolution analysis for the non-uniform model for the Ingólfsfjall (left-hand panel) and the Kross fault (right-hand panel), using GPS data only (first row), InSAR data only (second row), and GPS and InSAR (third row). Contours show the preferred slip distribution. The colour scale indicates the level of resolution, with one well-resolved areas and zero unresolved areas. Both fault are reasonably well resolved (>0.1) down to ~6 km depth, where most of the coseismic slip is inferred.
Table S1. Coseismic GPS station offsets.
Table S2. Selected InSAR interferograms spanning the 2008 May 29 earthquakes.

Please note: Wiley-Blackwell are not responsible for the content or functionality of any supporting materials supplied by the authors. Any queries (other than missing material) should be directed to the corresponding author for the article.